Received <day> <Month>, <year>; | Revised <day> <Month>, <year>; | Accepted <day> <Month>, <year>

DOI: xxx/xxxx

RESEARCH ARTICLE

Numerical Prediction of Turbulent Boundary Layer Noise from a Sharp-Edged Flat Plate

Mahmoud Karimi*[1,2] | Paul Croaker[1] | Alex Skvortsov[3] | Danielle Moreau[1] | Nicole Kessissoglou[1]

[1]School of Mechanical and Manufacturing Engineering, The University of New South Wales, Sydney, Australia

[2]Centre for Audio, Acoustics and Vibration, University of Technology Sydney, Sydney, Australia

[3]Maritime Division, Defence Science and Technology, Melbourne, Australia

Correspondence
*Mahmoud Karimi
Email: Mahmoud.Karimi@uts.edu.au

Present Address
Centre for Audio, Acoustics and Vibration, University of Technology Sydney, Sydney, Australia

Abstract

An efficient hybrid uncorrelated wall plane waves (UWPW)-boundary element method (BEM) technique is proposed to predict the flow-induced noise from a structure in low Mach number turbulent flow. Reynolds-averaged Navier-Stokes (RANS) equations are used to estimate the turbulent boundary layer parameters such as convective velocity, boundary layer thickness and wall shear stress over the surface of the structure. The spectrum of the wall pressure fluctuations is evaluated from the turbulent boundary layer parameters and by using semi-empirical models from literature. The wall pressure field underneath the turbulent boundary layer is synthesized by realisations of uncorrelated wall plane waves. An acoustic BEM solver is then employed to compute the acoustic pressure scattered by the structure from the synthesized wall pressure field. Finally, the acoustic response of the structure in turbulent flow is obtained as an ensemble average of the acoustic pressures due to all realisations of uncorrelated plane waves. To demonstrate the hybrid UWPW-BEM approach, the self-noise generated by a flat plate in turbulent flow with Reynolds number based on chord $Re_c = 4.9 \times 10^5$ is predicted. Results are compared with those obtained from a large eddy simulation (LES)-BEM technique, as well as with experimental data from literature.

KEYWORDS:
Flow-Induced Noise; computational fluid dynamics; boundary element method; uncorrelated wall plane waves; turbulent boundary layer

1 | INTRODUCTION

Prediction of flow-induced noise is required for a wide range of applications including gas-turbine blades, helicopter rotors, wind turbines, cooling fans and aircraft wings. The only numerical approach that can simultaneously resolve flow structure, flow noise sources, and capture the scattered and radiated sound from the body in the flow is direct numerical simulation (DNS)[1]. However, DNS is computationally extremely expensive, particularly at high Reynolds number as the entire range of spatial and temporal scales of the turbulence are resolved. Even with high performance computers and the ability to store large quantities of data, a single relatively simple model can still take several months to solve. As such, DNS is not suitable to examine the effect of design modifications for a range of operating conditions on flow noise predictions. An alternative approach is to consider splitting techniques corresponding to hybrid hydrodynamic/acoustic methods in which flow noise sources are extracted from CFD data and applied as an input to an acoustic analogy to predict the scattered and radiated sound by a body immersed in the flow.

Hybrid LES-acoustic analogy techniques have been developed that provide a high fidelity approach to predict the flow induced noise from a body submerged in the flow[2,3,4,5,6,7]. The LES simulations are able to capture the fluctuating flow noise sources with great detail over a wide range of frequencies. An incompressible large eddy simulation was performed by Wang and Moin[2] to simulate turbulent flow over a flat strut, with the predicted hydrodynamics comparing well with experimental results reported by Blake[8]. Seo and Moon[4] developed a modified version of the perturbed compressible equations known as the linearised perturbed compressible equation (LPCE). They showed that the LPCE method can accurately predict the sound pressure field radiated from turbulent flow past a cylinder. Moon et al.[9] investigated the flow-generated noise from a flat plate at zero angle of attack in subsonic turbulent flow using a hybrid LES-LPCE technique. Manoha et al.[10] performed LES of trailing edge flow and computed the radiated noise using Lighthill's acoustic analogy. Compared to DNS, the computational cost using LES is reduced by ignoring the smallest length scales of the turbulence. However even using LES to resolve the transient hydrodynamic flow field around a body for high Reynolds numbers still requires long simulation run times and large data storage requirements. The development of efficient methods that are able to predict flow noise characteristics while preserving the turbulent flow physics forms the motivation for the current work.

Statistical models have been proposed to predict flow noise sources using mean flow data from a steady-state RANS solution[11,12]. RANS is capable of predicting mean values of turbulent boundary layer parameters with good fidelity, even for complicated geometries and range of flow conditions. Two main methods are usually used in conjunction with RANS data to predict flow-induced noise sources. In the first method, termed the synthetic turbulence reconstruction method, RANS mean flow data is applied to reconstruct a turbulent velocity flow field. For example, the stochastic noise generation radiation method which is based on random Fourier modes uses a RANS solution to generate an instationary turbulent velocity field with the same local statistical properties as the RANS solution[11]. This generated turbulent field is then used for evaluating source terms in the linearized Euler equations[13] or using an acoustic analogy (for example, see Refs[14,15]). Airframe and jet noise sources were modelled using the random particle-mesh method introduced by Ewert[16], which is capable of reconstructing a turbulent velocity field from RANS data. However, subsequent calculation of flow noise sources from a reconstructed turbulent velocity flow field for a large CFD domain is very time consuming, thus defeating the motivation to conduct a RANS simulation. In the second method, RANS mean flow data is applied to predict the pressure fluctuations at the surface of a structure under a turbulent boundary layer[17]. Turbulent boundary layer (TBL) models that estimate surface pressure fluctuations include a single-point spectrum of wall pressure model and a wavenumber-frequency spectrum model. The single-point spectrum defines the frequency distribution at each point[18,19,20,21]. The wavenumber-frequency spectrum model provides the wavelength distribution[22,23,24,25,26]. Several hybrid RANS-acoustic analogy methods have been developed with specific application for trailing edge noise prediction in aeroacoustics by approximating the airfoil as an infinitely thin flat plate[27,28]. Maxit[29] modelled a vibrating panel excited by a turbulent boundary layer in which the wall pressure field from a TBL was simulated using realisations of uncorrelated wall plane waves (UWPWs). Using the UWPW technique, a good estimation of the panel response was obtained even when a relatively small number of realisations were considered. The UWPW technique is adopted here to synthesize the wall pressure field on the surface of a body immersed in turbulent flow, as an input to a model using the boundary element method to predict the far-field acoustic responses.

The boundary element method (BEM) is an efficient approach in computational acoustics for exterior problems in an unbounded fluid medium since it only requires the discretisation of the surface of the body, thus avoiding the need to discretise the acoustic domain. Hybrid CFD-BEM techniques applied to aeroacoustic scattering typically extract acoustic sources from transient CFD simulations[30,31]. In contrast, Ostertag et al.[32] extracted flow noise sources from steady-state RANS data rather

than transient CFD data. They then used a BEM technique to predict the aeroacoustic scattering from the trailing edge of an airfoil. The BEM was implemented by Khalighi et al.[33] to derive a boundary integral equation from Lighthill's wave equation. The method was applied to predict the sound pressure field radiated by turbulent flow past a cylinder and an automotive side mirror, as well as the trailing edge noise from an airfoil[33]. For all cases, the predicted radiated sound field matched well with experimental measurements. Croaker et al.[34] presented a particle accelerated hybrid CFD-BEM technique to predict low Mach number flow induced noise, the scattering of this noise by a body immersed in the flow and the resulting far-field sound pressure. The hybrid CFD-BEM technique was performed to predict the vortex shedding sound waves scattered by a two-dimensional cylinder[6]. The scattered far-field sound pressure was shown to compare well with results obtained using Curle's analogy for acoustically compact bodies.

This work presents an efficient aeroacoustic numerical method for prediction of flow induced noise from structures in low Mach number turbulent flow using a hybrid UWPW-BEM technique. The mean flow and turbulence statistics of the flow over a structure are predicted using an incompressible RANS simulation. The novelty of the proposed technique is the coupling between the hydrodynamics and acoustics solvers using an uncorrelated wall plane wave technique to synthesize the fluctuating pressures on the surface of the structure from the RANS data. To ensure that the turbulent flow physics were accurately captured, a range of models for the auto and normalised cross spectrum functions were implemented to compute the cross spectrum of the wall pressure. Each realisation of the synthesized wall pressure field was then used as the input to a BEM model of the body, from which the acoustic response for that realisation was predicted. The total acoustic response due to flow-induced noise from the body in a turbulent flow field was then obtained from an ensemble average for the number of realisations considered. The effects of the number of realisations on the synthesized wall pressure, incident pressure field from the turbulent boundary layer, and far-field scattered pressure are explored. The efficiency of the proposed approach is three-fold. First, the hydrodynamic simulation run time to resolve the fluid dynamics is significantly reduced using RANS compared to LES. Second, an acoustic solver based on the BEM requires discretisation of the acoustic domain on the surface of the structure. As such, only pressure spectra on the surface of the body need to be estimated. Third, the hydrodynamics and acoustics techniques are efficiently coupled using wall pressure spectra from the uncorrelated wall plane wave technique. The accuracy of the proposed UWPW-BEM approach is validated against data obtained from a hybrid LES-BEM solver as well as experimental data measured in the anechoic wind tunnel at the University of Adelaide.

2 | HYBRID UWPW-BEM TECHNIQUE

Figure 1 illustrates the computational sequences for the UWPW-BEM approach using the RANS simulation. First, a CFD mesh is created from the geometry in a CFD solver. A RANS simulation is performed to estimate the turbulent boundary layer parameters (convective velocity, boundary layer thickness, displacement thickness, momentum thickness and wall shear stress) over the surface of a structure for a given geometry and flow condition. The cross spectrum of the wall pressure is evaluated from the turbulent boundary layer parameters using semi-empirical models. The spectra of the wall pressure is then applied in conjunction with the UWPW technique to obtain the wall pressure field. The wall pressure field is then used as an input to the BEM acoustic solver. Within the BEM, the scattered acoustic pressure is computed using the generalized minimal residual (GMRES) method which is an efficient iterative solver[35]. This process is repeated for each realisation of the wall pressure field. Finally, the acoustic response of the system is obtained from an ensemble average of the different realisations of the wall pressure fields at each frequency. The methodology for the sequences is presented in what follows.

2.1 | Reynolds-averaged Navier-Stokes simulation

To resolve the fluid dynamics, a steady-state RANS simulation is conducted. Using Reynolds decomposition, the solution variables in the Navier-Stokes equations are decomposed into their mean and fluctuating components. The instantaneous velocity is written as $u_i = \overline{u}_i + u_i'$, where $\overline{u}_i$ and u_i' are respectively the mean and fluctuating velocity components. Similarly, other scalar quantities such as pressure and energy are decomposed into their mean and fluctuating components. Substituting expressions of this form for the flow variables into the instantaneous continuity and momentum equations and taking a time average yields the time-averaged momentum equations, which can be written in the following Cartesian tensor form[36]

$$\frac{\partial}{\partial x_i}\left(\overline{u}_i\right) = 0 \tag{1}$$

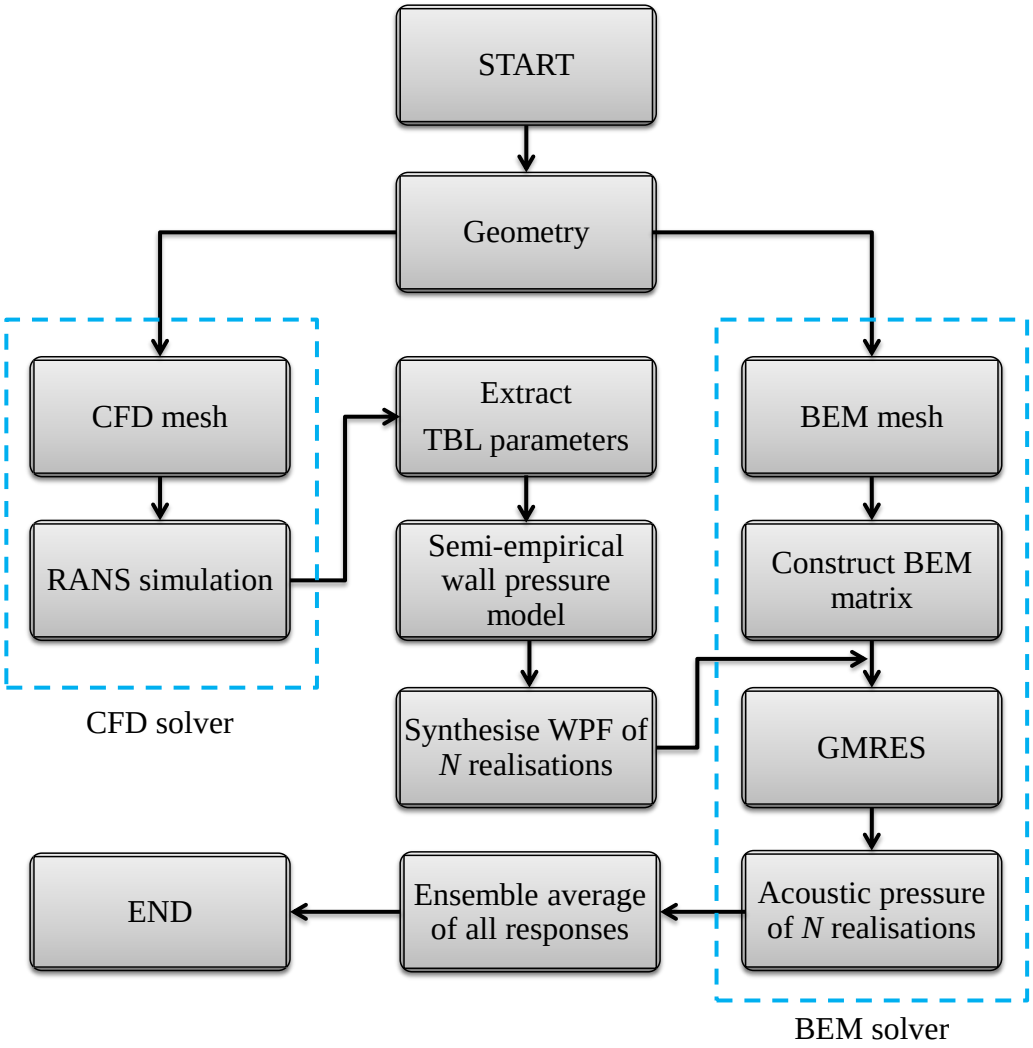

FIGURE 1 Flowchart of the computational process for the UWPW-BEM approach using uncorrelated wall plane waves (TBL = turbulent boundary layer, WPF = wall pressure field).

$$\rho_f \frac{\partial}{\partial x_i}(\overline{u}_i \overline{u}_j) = -\frac{\partial \overline{p}}{\partial x_j} + \frac{\partial}{\partial x_i}\left(\mu\left(\frac{\partial \overline{u}_i}{\partial x_j} + \frac{\partial \overline{u}_j}{\partial x_i} - \frac{2}{3}\delta_{ij}\frac{\partial \overline{u}_l}{\partial x_l}\right)\right) + \frac{\partial R_{ij}}{\partial x_i} \tag{2}$$

where $\overline{p}$ is the mean pressure, ρ_f is the fluid density and R_{ij} are the Reynolds stresses. Equations (1) and (2) are Reynolds-averaged Navier-Stokes equations. In general, they are in the same form as the instantaneous Navier-Stokes equations, with the velocities and other solution variables now representing time-averaged values. The Reynolds stress terms are modelled using functions containing empirical constants and information about mean flow. Many different turbulence models have been developed and since none of them are expected to be universally valid for all types of flows, a suitable model should be implemented based on the geometry of the struture and turbulent flow under investigation. Turbulent boundary layer parameters corresponding to convective velocity, boundary layer thickness and wall shear stress are extracted from the CFD data in order to synthesize the wall pressure fluctuations on the surface of the body using the uncorrelated wall plane wave technique.

2.2 | Uncorrelated wall plane wave technique

The uncorrelated wall plane wave technique recently introduced by Maxit[29] is used to simulate the pressure field beneath a turbulent boundary layer using realisations of UWPWs. The UWPW approach is summarized in what follows. The space-frequency cross spectrum of the wall pressure fluctuations is given by[37,29]

$$S_{pp}^{\mathrm{TBL}}(\mathbf{x}-\mathbf{x}',\omega)=\Psi_{pp}(\omega)\left(\frac{U_c}{\omega}\right)^2\tilde{S}_{pp}(\mathbf{x}-\mathbf{x}',\omega) \tag{3}$$

where $\Psi_{pp}(\omega)$ and $\tilde{S}_{pp}(\mathbf{x}-\mathbf{x}',\omega)$ are respectively the auto spectrum density (ASD) function and normalized cross spectrum density (CSD) function of the pressure field. U_c is the convective velocity and ω is the angular frequency. The wall pressure spectrum in the physical space is related to the wall pressure spectrum in the wavenumber space $\phi_{pp}(\mathbf{k},\omega)$ by the space Fourier transform as follows

$$S_{pp}^{\mathrm{TBL}}(\mathbf{x}-\mathbf{x}',\omega)=\frac{1}{4\pi^2}\int_{\infty}\phi_{pp}(\mathbf{k},\omega)e^{\mathrm{i}\mathbf{k}(\mathbf{x}-\mathbf{x}')}d\mathbf{k} \tag{4}$$

where $\mathrm{i}=\sqrt{-1}$ is the imaginary unit and $\mathbf{k}$ is the wavevector with components of k_x and k_y in the streamwise and spanwise directions, respectively. The improper integral in this transformation can be approximated using the rectangular rule by truncating and regularly sampling the wavenumber space as follows

$$S_{pp}^{\mathrm{TBL}}(\mathbf{x}-\mathbf{x}',\omega)\approx\frac{1}{4\pi^2}\sum_{i=1}^{p}\sum_{j=1}^{q}\phi_{pp}(k_x^i,k_y^j,\omega)e^{\mathrm{i}\mathbf{k}(\mathbf{x}-\mathbf{x}')}\delta k_x\delta k_y \tag{5}$$

where δk_x, δk_y are the wavenumber resolutions in the streamwise and spanwise directions, respectively. The total pressure beneath a turbulent boundary layer can be represented by a set of UWPWs. Hence, the CSD function of the pressure induced by this set of wall plane waves can be written as

$$S_{pp}^{\mathrm{UWPW}}(\mathbf{x}-\mathbf{x}',\omega)=\sum_{i=1}^{p}\sum_{j=1}^{q}(S_{AA})_{ij}e^{\mathrm{i}\mathbf{k}(\mathbf{x}-\mathbf{x}')} \tag{6}$$

where $(S_{AA})_{ij}$ are the stochastic amplitudes of the UWPWs. Equations (5) and (6) allow the CSD function of the pressure field by the TBL to be approximately equal to the CSD function of the UWPWs if the amplitudes of the UWPWs are defined by

$$(S_{AA})_{ij}=\frac{\phi_{pp}(k_x^i,k_y^j,\omega)\delta k_x\delta k_y}{4\pi^2}. \tag{7}$$

The amplitude of each wall pressure plane wave is in fact defined such that the whole set can represent the statistical properties of a wall pressure field generated by a TBL.

The wall pressure fluctuations beneath the turbulent boundary layer using the UWPW technique for the n^{th} realisation at the l^{th} node can be expressed by[29]

$$p_{\mathrm{inc}}^{n}(\mathbf{x}^l,\omega)=\sum_{i=1}^{p}\sum_{j=1}^{q}\sqrt{\frac{\phi_{pp}(k_x^i,k_y^j,\omega)\delta k_x\delta k_y}{4\pi^2}}e^{\mathrm{i}(k_x^ix^l+k_y^jy^l+\varphi_{ij}^n)} \tag{8}$$

$$\phi_{pp}(k_x,k_y,\omega)=\Psi_{pp}(\omega)\left(\frac{U_c}{\omega}\right)^2\tilde{\phi}_{pp}(k_x,k_y,\omega) \tag{9}$$

where x, y respectively represent the axes in the streamwise and spanwise directions. $\tilde{\phi}_{pp}(k_x,k_y,\omega)$ is the normalized CSD of the wall pressure field and φ is a random phase uniformly distributed in $[0\ \ 2\pi]$. Note that $\Psi_{pp}(\omega)$ is a one-sided radial frequency spectrum, $\Psi_{pp}(\omega)$ was multiplied by 2π to convert it to a one-sided cyclic frequency spectrum density $\Psi_{pp}(f)$.

The cross spectrum of the wall pressure can be computed using different models for the auto spectrum function and the normalised cross spectrum function independently from each other. In this work, the Goody[20] model was used for the auto spectrum function and the Chase[23], Corcos[22] and generalized Corocs models[26] were considered for the normalised cross spectrum function. Equation (8) is then used to synthesize the TBL pressure fluctuations on the surface of a structure. Prediction of the pressure scattered by the structure using the BEM for each realisation of the wall pressure field obtained from the UWPW technique is described in the proceeding section.

2.3 | Boundary element method

Assuming a time harmonic dependence of the form $e^{-i\omega t}$, the Helmholtz equation is given by

$$\Delta p_f(\mathbf{x},\omega) + k_f^2 p_f(\mathbf{x},\omega) = -S, \tag{10}$$

where $p_f(\mathbf{x},\omega)$ is the acoustic pressure at field point $\mathbf{x}$, Δ is the Laplacian operator, $k_f = \omega/c_f$ is the acoustic wave number, c_f is the speed of sound and S is the source. Equation (10) can be written as a boundary integral equation after integrating by parts twice and using Green's theorem as follows[38]

$$c(\mathbf{x})p_f(\mathbf{x},\omega) + \int_\Gamma \frac{\partial G(\mathbf{x},\mathbf{y},\omega)}{\partial n(\mathbf{y})} p_f(\mathbf{y},\omega)\,\mathrm{d}\Gamma(\mathbf{y}) = i\omega\rho_f \int_\Gamma G(\mathbf{x},\mathbf{y},\omega) v_f(\mathbf{y},\omega)\,\mathrm{d}\Gamma(\mathbf{y}) + p_{\text{inc}}(\mathbf{x},\omega) \tag{11}$$

where Γ is the boundary surface of the body. The vector $\mathbf{n}(\mathbf{y})$ represents the outward normal vector at the source point $\mathbf{y}$ and $\partial/\partial n(\mathbf{y})$ is the normal derivative. $v_a(\mathbf{y})$ is the fluid particle velocity and is related to the normal derivative of the acoustic pressure as follows

$$v_f(\mathbf{y},\omega) = \frac{1}{i\omega\rho_f} \frac{\partial p_f(\mathbf{y},\omega)}{\partial n(\mathbf{y})}. \tag{12}$$

$p_{\text{inc}}(\mathbf{x},\omega)$ is the acoustic pressure incident as a result of the acoustic source. $c(\mathbf{x})$ is a free-term coefficient and equals 1 in the domain interior and 0.5 on a smooth boundary. $G(\mathbf{x},\mathbf{y},\omega)$ is the free-space Green's function for the Helmholtz equation given by

$$G(\mathbf{x},\mathbf{y},\omega) = \frac{e^{ik_f r}}{4\pi r} \qquad \text{where} \qquad r = \|\mathbf{x}-\mathbf{y}\|. \tag{13}$$

For a rigid structure, the fluid particle velocity at the surface of the structure is zero, that is, $v_f(\mathbf{y},\omega) = 0,\ \mathbf{y} \in \Gamma$. In order to predict the acoustic pressure in the domain, the pressure on the surface of the scatterer has to be initially determined. The surface of the scatterer was discretised using discontinuous quadrilateral elements due to their super convergence. The acoustic pressure on each element is then expressed using interpolation functions and the nodal values as follows[38]

$$p_f(\mathbf{y},\omega) = \sum_{i=1}^{M} \Phi_i(\mathbf{y}) p_i(\omega) \tag{14}$$

where $\Phi_i(\mathbf{y})$ are interpolation functions, M is the number of nodal points in each element and p_i represents the acoustic pressure at nodal points. Substituting equation (14) into equation (11), the BEM formulation is obtained as a linear system of equations given by

$$\mathbf{H}\mathbf{p}_i = \mathbf{p}_{\text{inc}} \tag{15}$$

where $\mathbf{H}$ is the BEM coefficient matrix and is complex and non-symmetric. Vectors $\mathbf{p}_i$ and $\mathbf{p}_{\text{inc}}$ respectively represent the acoustic pressure and incident pressure at nodal points. Once the scattered pressure on the surface of the structure is obtained using equation (15), the far-field acoustic pressure $p_f^n(\mathbf{x},\omega)$ for the n^{th} realisation is computed as follows

$$p_f^n(\mathbf{x},\omega) = -\mathbf{h}\mathbf{p}_i \tag{16}$$

where $\mathbf{h}$ is the BEM far-field matrix. The aforementioned process is repeated for each realisation of the wall pressure field. The scattered acoustic response is then obtained from the ensemble average of the responses computed for the number of realisations considered at each frequency as follows

$$S_{pp}^N(\mathbf{x},\omega) = \mathbf{E}\left[p_f^n(\mathbf{x},\omega)(p_f^n(\mathbf{x},\omega))^*\right]_{n\in\{1,\ldots,N\}} \tag{17}$$

where $\mathbf{E}$ represents the ensemble average over the number of realisations and the asterisk * denotes the complex conjugate.

3 | HYBRID LES-BEM TECHNIQUE

To validate the proposed UWPW-BEM approach, a hybrid LES-BEM technique is employed to predict the interaction of flow induced noise with a body submerged in turbulent flow. Figure 2 illustrates the numerical procedure in the hybrid LES-BEM technique. The geometry of the CFD domain is initially created. The CFD domain is meshed and implemented in a transient CFD simulation. Velocity components from the simulation are extracted to calculate the flow noise sources. Since these sources are in the time domain, a discrete Fourier transform (DFT) is performed to convert the data into the frequency domain. Next, the incident pressure on the surface of the structure due to the flow noise sources is predicted using Lighthill's acoustic analogy

and used as an input to the BEM solver. In the BEM, the geometry of the scatterer is meshed using discontinuous quadrilateral elements. The scattered acoustic pressure is computed using the GMRES method. Finally, the scattered field is added to the direct field from the flow noise sources to generate the total acoustic pressure.

LES is governed by filtered Navier Stokes equations as follows[39]

$$\frac{\partial}{\partial x_i}\left(\tilde{u}_i\right) = 0 \tag{18}$$

$$\frac{\partial \tilde{u}_i}{\partial t} + \frac{\partial(\tilde{u}_i\tilde{u}_j)}{\partial x_j} = -\frac{1}{\rho_f}\frac{\partial \tilde{p}}{\partial x_i} + \frac{\partial}{\partial x_j}\left(\nu\frac{\partial \tilde{u}_i}{\partial x_j}\right) - \frac{\partial \tau_{ij}}{\partial x_j} \tag{19}$$

where $\tilde{u}$ and $\tilde{p}$ are resolved-scale components of velocity and pressure, respectively. $\tau_{ij} = \rho_f(\widetilde{u_i u_j} - \tilde{u}_i\tilde{u}_j)$ are subgrid-scale turbulent stresses. The analysis was performed at low Mach number for which the flow can be well approximated by the incompressible Navier-Stokes equations. Further, the effect of background mean flow on the scattered sound was neglected as it was found to have negligible effect on far-field sound at low Mach number[40].

Calculation of noise sources using velocity components extracted from the LES simulation is described in what follows. The source S in equation (10) is replaced with a double spatial derivative of Lighthill's tensor[14]

$$S = \frac{\partial^2 T_{ij}}{\partial y_i \partial y_j} \tag{20}$$

where $T_{ij} = \rho_f u_i u_j$ is the approximate Lighthill's tensor (at low Mach number), and u_i, u_j are the i^{th} and j^{th} components of the instantaneous velocity vector, respectively. The particular solution of the non-homogenous Helmholtz equation due to this source can be expressed by

$$p_{\text{inc}}(\mathbf{x},\omega) = \int_{\Omega} \frac{\partial^2 T_{ij}(\mathbf{y})}{\partial y_i \partial y_j} G(\mathbf{x},\mathbf{y},\omega)\,\mathrm{d}\mathbf{y} \tag{21}$$

where Ω is the computational domain. Equation (21) was solved using formulations for the near-field pressure which is described in detail by Croaker et al.[31]. The solution of equation (21) inside the source region is the total pressure, which includes both hydrodynamic and acoustic contributions. Applying this total pressure as an incident field to a BEM model of the scatterer has been previously shown to produce accurate far-field sound predictions[6,33].

4 | RESULTS AND DISCUSSION

A flat plate considered in the experiment conducted by Moreau et al.[41,42] in an anechoic wind tunnel was modelled here as a rigid structure. Therefore, the vibration of the plate due to the hydrodynamic pressure is neglected. The plate has a chord of 200 mm, a span of 450 mm, and a thickness of 5 mm. The leading edge is circular with a diameter of 5 mm while the trailing edge is a symmetric wedge shape with an apex angle of 12° as shown in figure 3. The experimental setup for the plate in the anechoic wind tunnel is shown in figure 4. The anechoic wind tunnel contains a contraction outlet that is rectangular in cross section and has dimensions of 75 mm × 275 mm. The span of the plate extended beyond the width of the contraction outlet to eliminate the noise produced by the interaction of the side plate boundary layers with the leading edge. The plate was tested with zero angle of attack and the radiated sound pressure was measured at 585 mm above the trailing edge.

4.1 | Hydrodynamic results

4.1.1 | CFD model

Incompressible flow past the plate was simulated at a Reynolds number based on chord Re_c=4.9×10^5 and Mach number M=0.1. At this Reynolds number, the flow was in the turbulent unsteady regime and was three dimensional. A C-grid computational domain was used to minimize the boundary condition influence, which was extended two chords above and below the plate, two chords upstream and three chords downstream, as shown in figure 5. A sponge layer extended the computational domain in the downstream direction for two chords with the cell size growing rapidly in the sponge layer in the streamwise direction. The sponge layer was implemented to allow the vortical disturbances in the wake to leave the computational domain smoothly. This was done by defining a cosine function in terms of x which increased the viscosity through the layer.

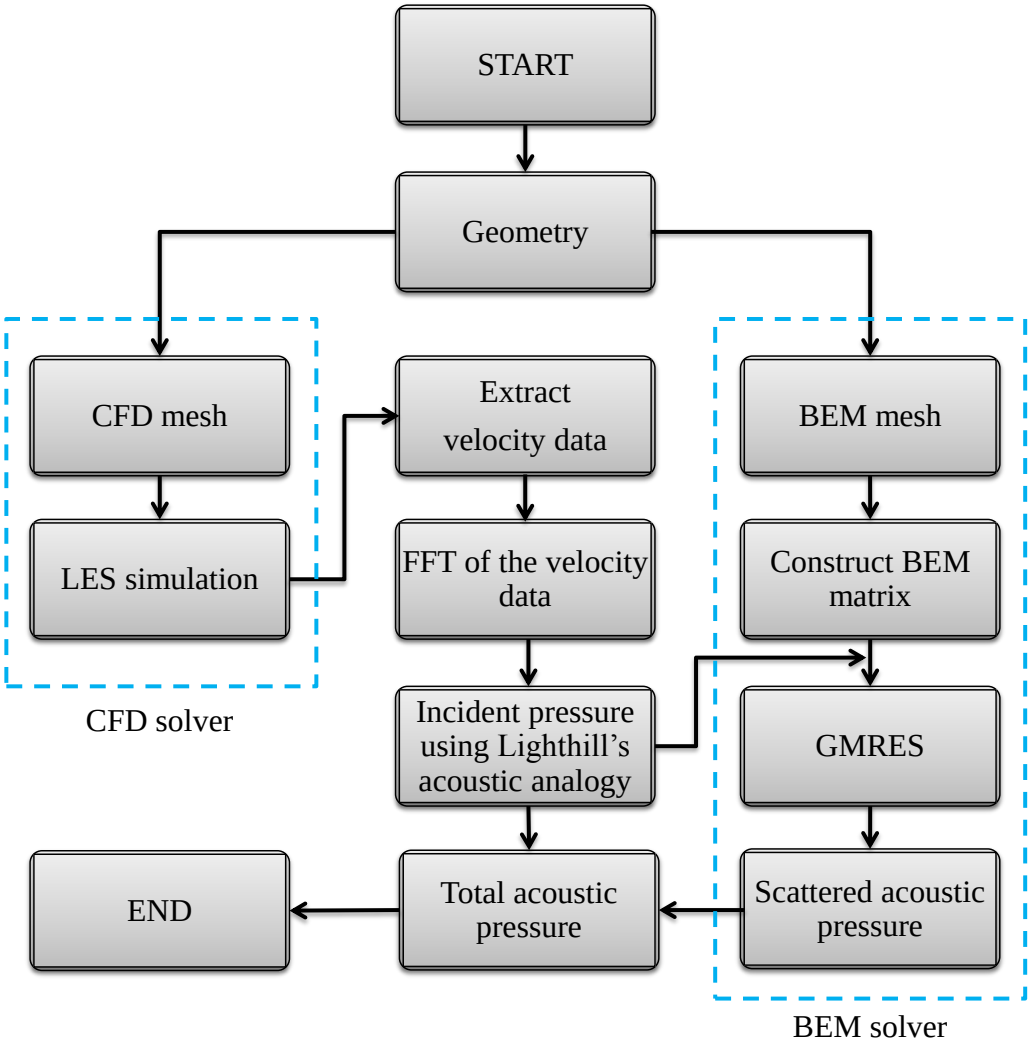

FIGURE 2 Flowchart of the computational process for the LES-BEM approach using Lighthill's acoustic analogy.

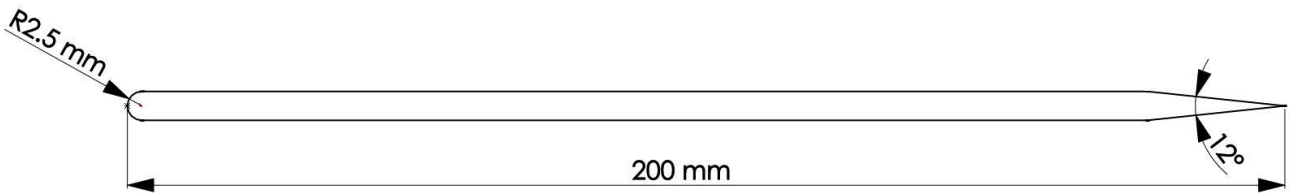

FIGURE 3 Sharp-edged flat plate dimensions

4.1.2 | RANS simulation

A single two-dimensional slice of the CFD model was used to perform a steady RANS simulation in Fluent based on Menter's shear-stress transport (SST) $k-\omega$ model. A pressure-based algorithm was employed to solve the RANS equation. The semi-implicit method for pressure-linked equations (SIMPLE) was used for pressure-velocity coupling. A second-order upwind scheme was used for the spatial discretization. The two-dimensional mesh contained approximately 320,000 quadrilateral cells. The sponge layer was inactive in the RANS simulation. The inlet velocity was set to 35 m/s on the semi-circular boundary, while

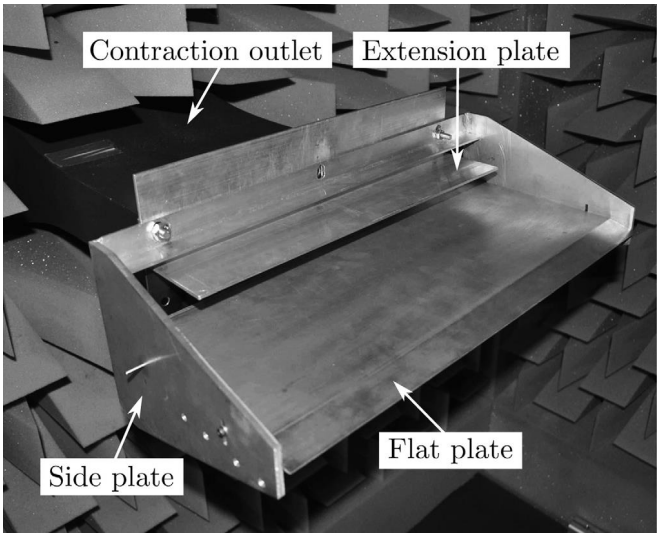

FIGURE 4 Experimental setup for the flat plate in the anechoic wind tunnel at the University of Adelaide[41]

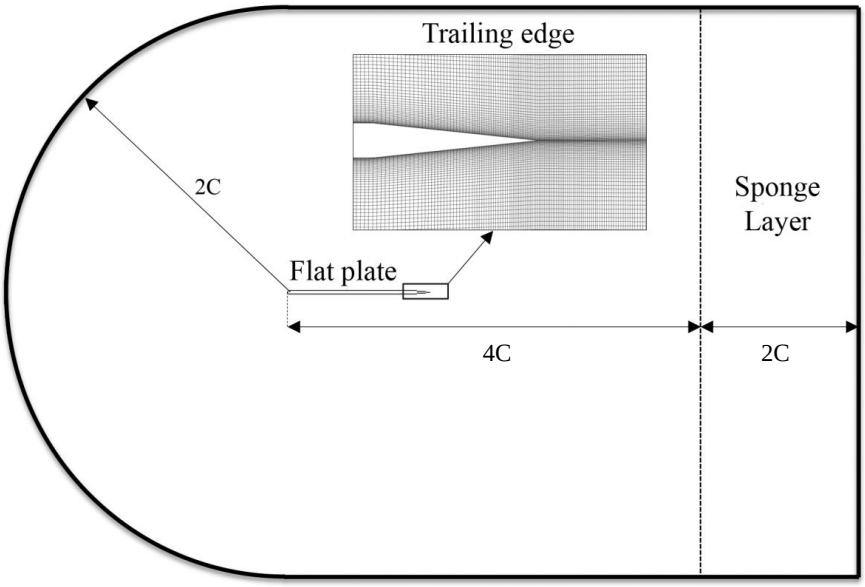

FIGURE 5 Schematic diagram of the shape and size of the CFD domain

a zero average pressure was imposed at the outlet. A no-slip condition was applied on the surface of the plate, and the top and bottom boundaries were considered as free-slip walls.

4.1.3 | LES simulation

The LES simulation was performed in Fluent in 3D with flow periodicity assumed at the side boundaries. The Smagorinsky-Lilly model was used to model the Subgrid scales in turbulence. A pressure-based segregated algorithm was employed to solve the non-linear and coupled governing equations sequentially. The pressure implicit with splitting of operators (PISO) algorithm was employed in the numerical simulations. The simulations were second-order accurate in time and space, with a bounded central difference scheme used for the spatial discretization and a bounded second-order scheme used for the temporal discretization.

A fully hexahedral mesh with approximately 10 million cells was created. The mesh distribution was biased so that the region near the plate and also the wake region contained high cell density to resolve eddies and fluctuations. Apart from the vicinity of the leading edge, the resolution of the near-wall grid on the plate in terms of wall unit was $\Delta x^+ \leq 29$, $\Delta y^+ \leq 1$ and $\Delta z^+ \leq 4.7$, where x, y and z respectively represent streamwise, wall-normal and spanwise directions. A spanwise extension was selected as 10% of the plate chord. The time step was 3×10^{-7}s and the maximum Courant-Friedrichs-Lewy number was 0.4. Prior to the LES simulation, a transient simulation based on Menter's shear-stress transport (SST) $k - \omega$ model was performed as an initial condition for the LES.

To visualize the flow structures within the boundary layer and at the trailing-edge, the Q-criterion as described by Chakraborty et al.[43] was employed. The Q-criterion corresponding to the second invariant of the velocity gradient tensor provides an indication of balance between strain rate and vorticity magnitude, and identifies vortices as regions where the vorticity magnitude is larger than the magnitude of strain rate. Figure 6 shows the iso-surfaces of the Q-criterion non dimensionalised by $(U_\infty/h)^2$, where h is the plate thickness and U_∞ is the free-stream velocity. The fluctuating flow structures in the boundary layer and wake produce pressure disturbances which interact with the surface of the plate and travel to the far field as sound.

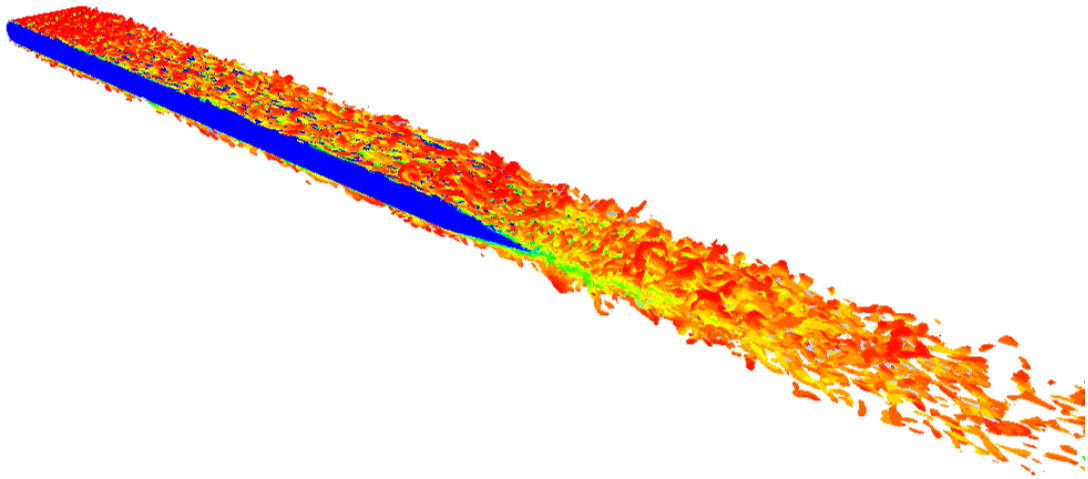

FIGURE 6 Flow structures over the flat plate at $Re_c = 4.9 \times 10^5$ and Mach number $M = 0.1$; Iso-surface of $Q = 0.2$, non dimensionalised by $(U_\infty/h)^2$

The instantaneous spanwise vorticity over the flat plate is shown in figure 7. To illustrate the effectiveness of the sponge layer at damping out the vorticity, a vertical line has been drawn which denotes the location where the sponge layer begins. It can be seen that the vorticity contours are smoothly reduced in magnitude through the sponge layer, with no reflection evident from the downstream boundary.

4.1.4 | Velocity profile and spectral map

A comparison between the near wake mean velocity profile extracted from LES and RANS simulations with the mean velocity profile obtained experimentally from the wind tunnel measurements is depicted in figure 8, where U is the mean velocity. Good

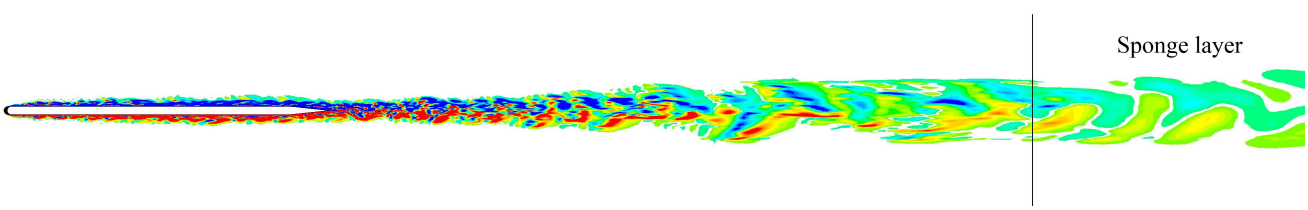

FIGURE 7 Instantaneous spanwise vorticity contours at the mid-span

agreement between numerical results obtained in this work and experimental results by Moreau et al.[42] can be observed. Figure 8 shows that the velocity profile is mostly symmetric about the trailing edge. Figure 9 compares the computed root-mean-square (RMS) fluctuating velocity with experimental results, where u' is the fluctuating velocity. The current LES model overpredicts the fluctuating velocity at the region near the trailing edge ($-0.1 < y/c < 0.1$). The velocity was measured in the vertical direction y at a constant x position of 0.6 mm from the trailing edge. Figure 10 presents the spectral map of the fluctuating velocity measured in the vertical direction at the trailing edge obtained experimentally and numerically using LES. The spectral maps indicate that the power spectral density of the fluctuating velocity is well predicted near the trailing edge for the entire range of frequencies. Significant low frequency turbulent fluctuations outside the plate boundary layer are observed in the experiments. This is attributed to the effect of the shear layer formed by the interaction of flow with the contraction outlet in the experiment.

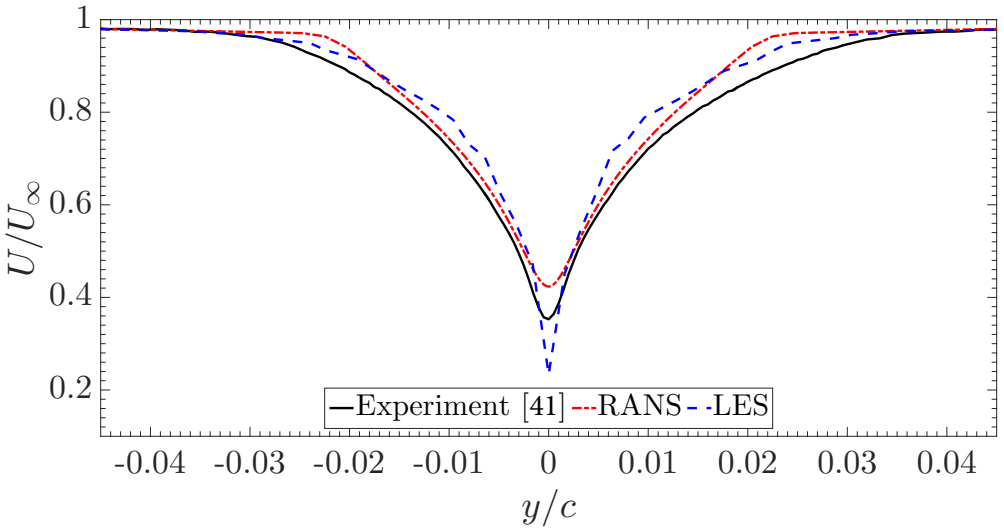

FIGURE 8 Normalized mean velocity profile (U/U_∞) measured in the near wake of the flat plate

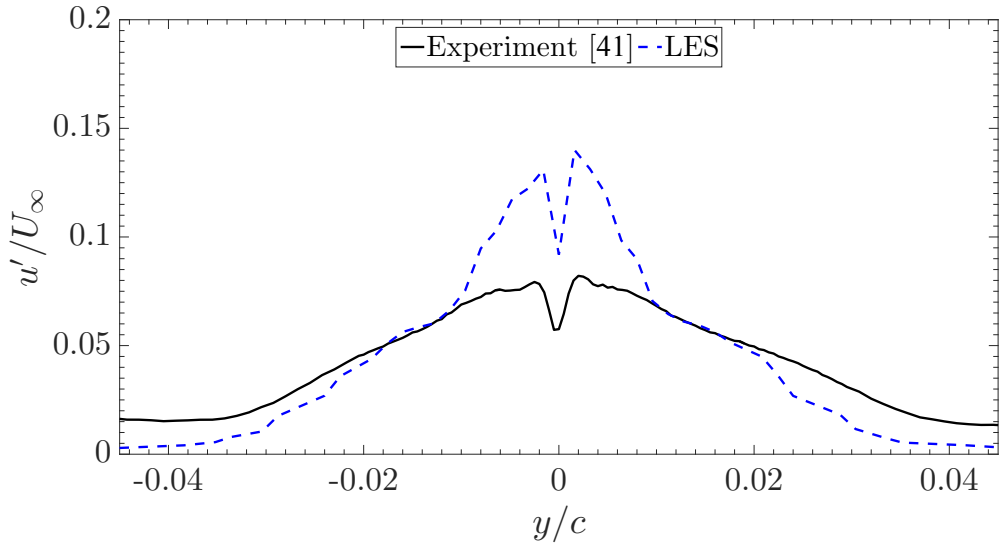

FIGURE 9 Normalized RMS velocity fluctuations $\overline{u}'/U_\infty$

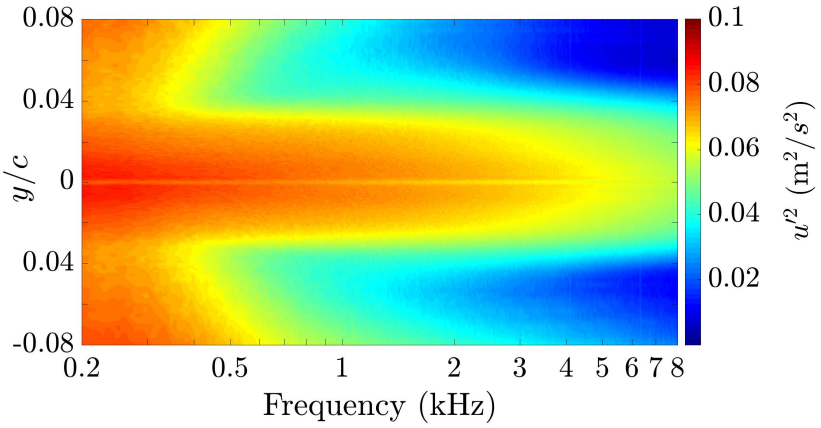

(a)

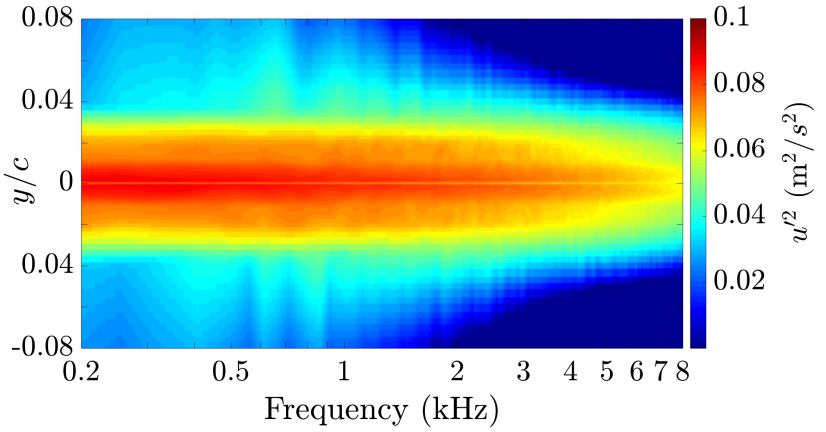

(b)

FIGURE 10 Spectral maps of the power spectral density of the fluctuating velocity measured near the trailing edge in the vertical direction at x/c=0.0035; (a) experimental results and (b) LES results

4.2 | Realisations of synthesized wall pressure field

The TBL parameters corresponding to the convective velocity, boundary layer thickness, displacement thickness, momentum thickness and wall shear stress were extracted from the RANS simulation and used to evaluate the cross spectrum density of the wall pressure field. The Goody model described in Appendix A was employed for the auto spectrum density function. The Chase, Corcos and generalized Corcos models as described in Appendix B were utilized for the normalized cross spectrum density function.

Although only 275 mm of the plate span was exposed to the contraction outlet, the incoming flow from the outlet affects a wider surface of the plate. To take into account this effect, a Hann window is applied to the wall pressure fluctuations over the surface of the plate as shown in figure 11. The coefficient of a Hann window was computed from the following equation

$$w(y) = \left\{ \begin{array}{ll} \frac{1}{2}\left(1 - \cos\left(2\pi \frac{y}{L_h}\right)\right), & y \leq L_h \\ 1, & L_h < y < (L_p - L_h) \\ \frac{1}{2}\left(1 - \cos\left(2\pi \frac{L_p - y}{L_h}\right)\right), & y \geq (L_p - L_h). \end{array} \right\} \tag{22}$$

According to this function, the magnitude of the surface pressure decreases with increasing distance from the contraction outlet and vanishes at the sides of the plate. This can be observed in figure 12 which presents two realisations of the wall pressure field on the surface of the flat plate at 0.6 kHz and 2.2 kHz using the Chase, Corcos and generalized Corcos models. The visualization of the surface pressure field in figure 12 shows that at low frequencies, a coarse mesh can resolve the waves as they have larger

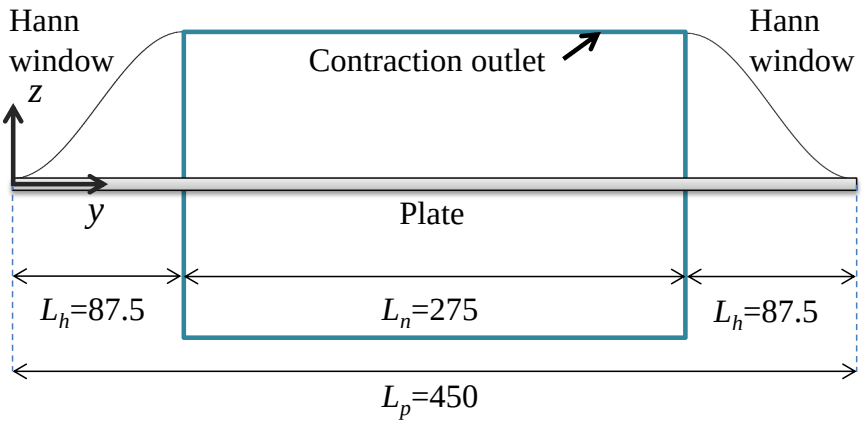

FIGURE 11 Hann window applied to the pressure field at the both sides of the contraction outlet (dimensions in mm)

wavelengths. However, at higher frequencies, a finer mesh is needed to properly describe and synthesize the wall pressure field for plane waves with short wavelengths. The criteria for choosing the mesh size is discussed later in the paper. Figure 12 shows that the wall pressure field pattern obtained using all three models are very similar. However, using the Chase model, a lower pressure field was obtained at low frequency (below 1 kHz) compared with other two models. Hence, it can be concluded that using the Chase model, the proposed method will produce far-field pressure of lower amplitude than the far-field pressure predicted using the Corcos or generalised Corcos models.

4.2.1 | Effect of the number of realisations on the synthesized wall pressure and the scattered pressure

To investigate the effect of the number of realisations on the wall pressure field, the Goody and Corcos models were implemented in equation (8) to estimate the pressure field at a single point at the trailing edge. Figure 13 shows the power spectral density of the TBL pressure as a function of frequency at the mid-span of the trailing edge (x, y, z)=(200, 222, 0) (dimensions in mm) for different realisations. It can be seen that the results become smoother as the number of realisations are increased. The effect of the number of realisations on the accuracy of the UWPW method was evaluated as follows. The result obtained using 300 realisations was selected as a converged solution and used as a reference to compute the discrepancy between results obtained with different numbers of realisations and is shown in figure 14. For the current case study, the average error using 30 realisations over the frequency range is less than 1 dB, which is an acceptable error from a practical point of view.

The effect of the number of realisations on the far-field scattered pressure at 585 mm above the trailing edge is shown in figure 15. It can be observed that increasing the number of realisations from 30 no longer changes the scattered pressure. As such, 30 realisations was used for all subsequent calculations. It should be noted that Maxit[29] also found that 30 realisations was enough to obtain the vibration response of a simply supported plate due to TBL excitation.

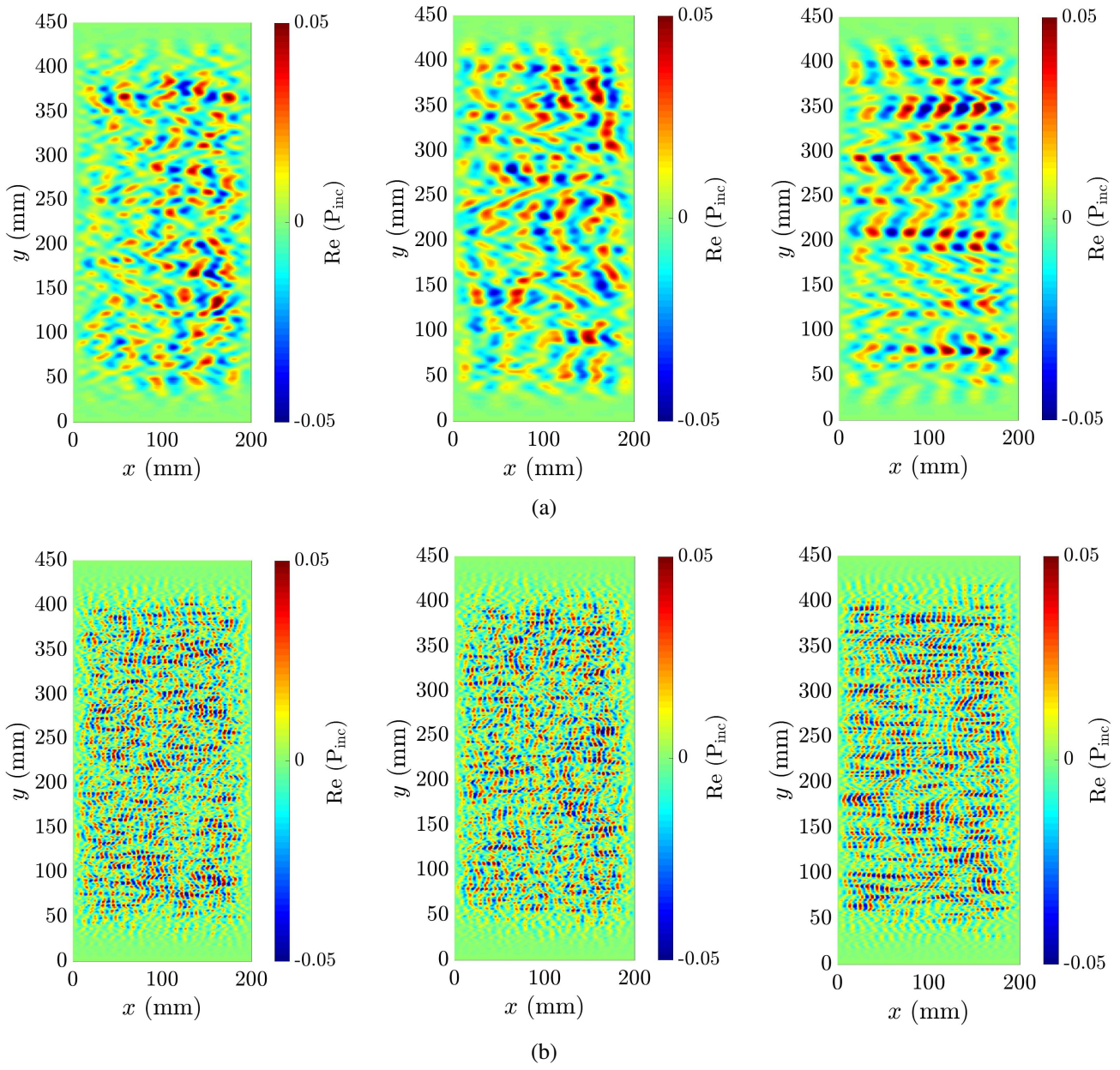

FIGURE 12 Two realisations of the wall pressure field at (a) 0.6 kHz and (b) 2.2 kHz using the Chase model (left), the Corcos model (middle) and the generalized Corcos model ($m = 1$ and $n = 2$)(right)

4.2.2 | Determination of cutoff wavenumbers and wavenumber resolutions

To correctly approximate the improper integral in the Fourier transform expressed by equation (4), criteria for choosing the cutoff wavenumbers and wavenumber resolutions need to be defined in both the streamwise and spanwise directions. Determination of the cutoff wavenumbers can be achieved by plotting the integrand of the integral as a function of wavenumber. Figure 16 presents the normalised cross spectrum function of the pressure field for the Chase, Corcos and generalized Corcos models at 4 kHz, for a free stream velocity of 35 m/s. Figure 16 (c) and (d) respectively correspond to the filter parameters ($m = 1, n = 2$) and ($m = 2$, $n = 1$) for the generalized Corcos model. According to figure 16, the highest values of the integrand occurs for wavenumbers close to the convective wavenumber $k_c = \omega/U_c$. The amplitude of the integrand decreases rapidly for wavenumbers significantly less or greater than k_c. An effective wavenumber range was selected such that the significant contributions of the integrands of all three models were taken into account. This was achieved by ensuring that the maximum estimated error in the calculation of

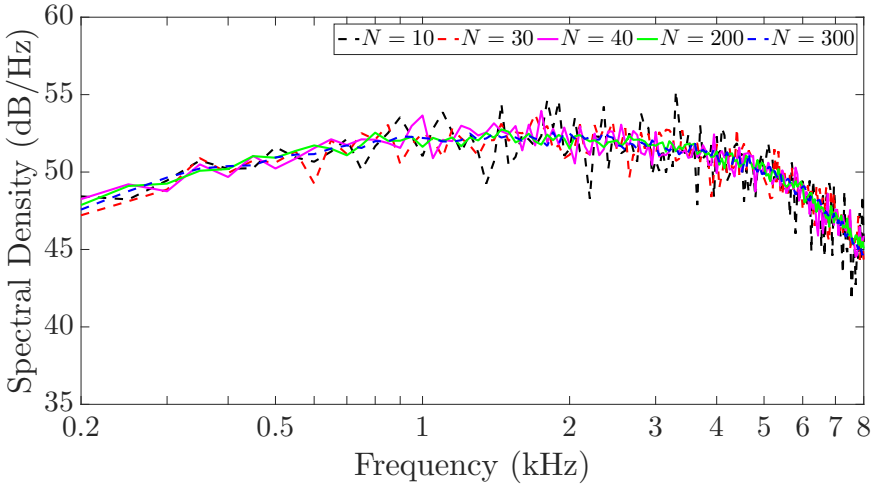

FIGURE 13 Spectral density of the incident pressure from the turbulent boundary layer at the mid-span of the trailing edge (x, y, z)=(200, 0, 222) for different realisations (dimensions in mm)

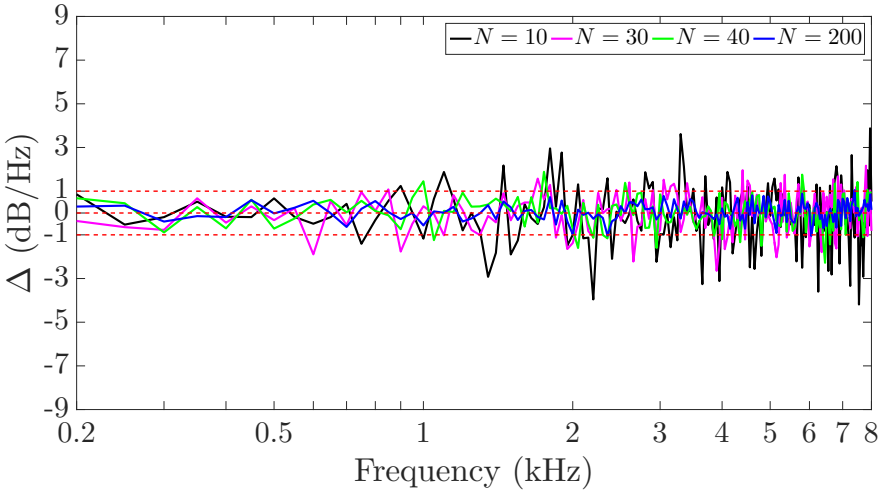

FIGURE 14 Difference in the spectral level of the surface pressure for different numbers of realisations using the results obtained with 300 realisations as the reference solution

the wall pressure field associated with the wavenumber domain truncation was less than 1 dB for the frequency range considered here. The selected wavenumber domain is shown in figure 16 and is given by

$$0 \leq k_x \leq 2k_c, \qquad -4k_c \leq k_y \leq 4k_c. \tag{23}$$

Since the cutoff wavenumbers are dependent on frequency and flow velocity, the criteria in equation (23) can be implemented at all frequencies for different flow conditions. Maxit[29] applied a trial and error process to find the constant wavenumber resolutions in the two directions to represent the spatial variations in the wavenumber space of the wall pressure spectrum. In this work, a frequency dependent increment in wavenumber is proposed which is assumed to be the same in both the streamwise and cross-stream directions, and which is given as follows

$$\delta k_x = \delta k_y = \beta k_c \tag{24}$$

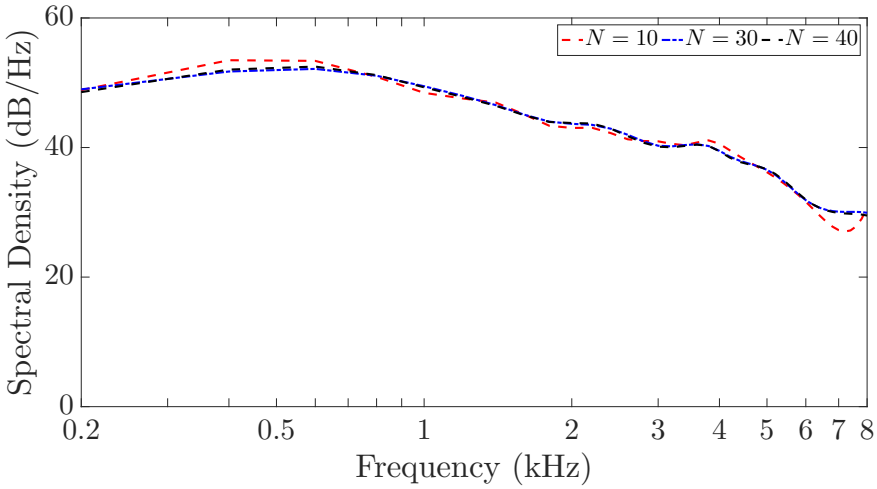

FIGURE 15 Far-field acoustic spectra of the scattered pressure for different numbers of realisations

where β is an increment coefficient. Figure 17 shows the effect of changing the increment coefficient on the scattered pressure above the trailing edge for the Chase and generalized Corcos models. Five different wavenumber resolutions were implemented in the numerical procedure. It was observed that using $\beta = 0.1$ and $\beta = 0.05$, the wavenumber resolutions were not fine enough to take into account the variation of the normalized CSD function of the wall pressure spectrum in wavenumber space. However, very similar results were obtained using $\beta = 0.01$, $\beta = 0.005$ and $\beta = 0.0025$, confirming that a converged scattered pressure was achieved. The increment coefficient of $\beta = 0.005$ was chosen for all subsequent calculations.

4.2.3 | Criteria for the mesh size

In order to properly capture the behaviour of the hydrodynamic field on the surface of structure, the mesh size needs to be carefully defined by taking into account the spatial distribution of the CSD function of the surface pressure. To synthesize the wall pressure field, the Nyquist sampling theorem for space and wavenumber was adopted. The sampling wavenumber is given by[44]

$$k_s = \frac{2\pi}{\Delta h}, \tag{25}$$

where Δh is the element size. According to the Nyquist theorem, the sampling wavenumber must be at least twice the highest wavenumber of interest, that is, $k_s = 2k_{c,\max}$. Substituting this expression into equation (25), the mesh size is given by

$$\Delta h = \frac{\pi}{k_{c,\max}}, \tag{26}$$

where $k_{c,\max}$ is the convective wavenumber at the highest frequency of interest. According to the criteria in equation (23) and considering the BEM mesh size requirement of at least 6 elements per acoustic wavelength, the grid size in the streamwise and spanwise directions can be defined as follows

$$\Delta x = \min\left(\frac{\pi}{2k_{c,\max}}, \frac{\pi}{3k_{a,\max}}\right), \qquad \Delta y = \min\left(\frac{\pi}{4k_{c,\max}}, \frac{\pi}{3k_{a,\max}}\right) \tag{27}$$

Surface pressure gusts can be classified as sub- or super-critical, respectively corresponding to subsonic and supersonic phase speeds of their trace along the leading/trailing edge with respect to the incident mean flow[45]. For a given flow condition, the Graham's parameter of less than or greater than unity corresponds respectively to sub-critical or super-critical pressure gusts. The Graham's parameter is given by Graham[46]

$$\Theta = \frac{M k_x}{\Lambda k_y} \tag{28}$$

where $M = U_\infty / c_a$ is the Mach number and $\Lambda = \sqrt{1 - M^2}$. Figure 18 shows the Graham's parameter in the wavenumber domain. For an infinite-span airfoil, the contribution of the sub-critical pressure gusts to the far-field scattered pressure is zero as they attenuate as evanescent waves away from the airfoil edges[47]. Although a finite-span plate is considered in this work,

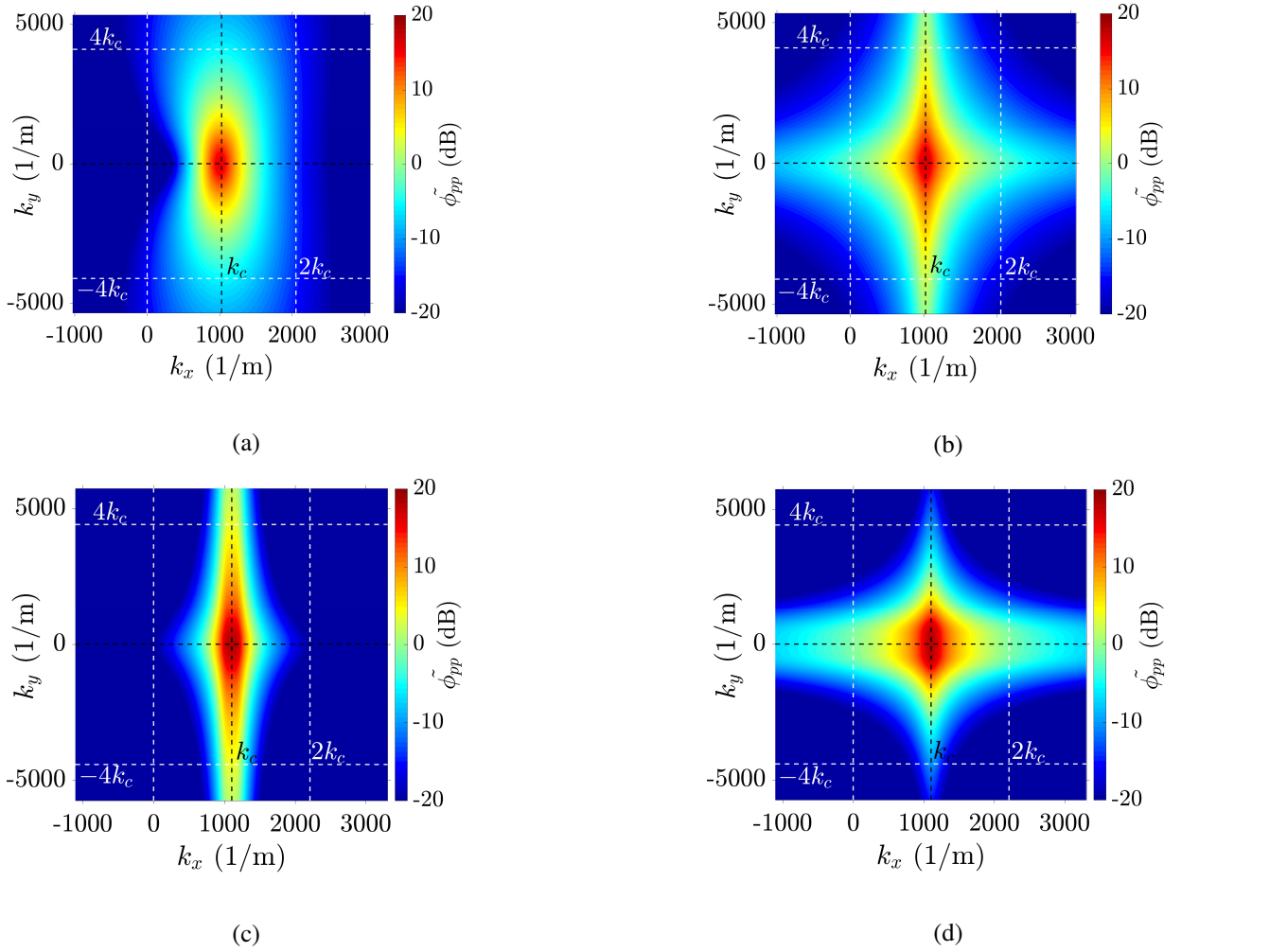

FIGURE 16 Colour map of normalized CSD function of the pressure field at 4 kHz. (a) Chase model, (b) Corcos model, (c) generalized Corcos model ($m = 1$ and $n = 2$), (d) generalized Corcos model ($m = 2$ and $n = 1$)

the contribution of the sub-critical gusts to the far-field scattered pressure is negligible as the Hann window has been applied to the incident pressure at the two sides of the contraction outlet, which forces the pressure gust magnitudes to zero at the plate spanwise ends. Hence, the criteria defined in equation (23) can be updated as follows

$$0 \leq k_x \leq 2k_c; \qquad -\frac{Mk_x}{\Lambda} \leq k_y \leq \frac{Mk_x}{\Lambda}. \tag{29}$$

Equation (29) implies that for a given k_x, k_y is varying between upper and lower bounds governed by two lines as depicted in figure 18. The pressure gusts with the wavenumbers confined to the triangular region (where $\Theta > 1$), which is formed by the vertical line at $k_x = 2k_c$. The two lines with the slope of $\pm M/\Lambda$ are super-critical gusts and are expected to dominate the scattered pressure. Using the criteria in equation (29), a much coarser mesh can be used in the spanwise direction than in streamwise direction. This is due to neglecting larger wavenumbers in the spanwise direction which have shorter wavelength. This can be demonstrated by visualizing the wall pressure field using the criteria in equation (29). Figure 19 shows two realisations of the wall pressure field at the same frequencies as those used in figure 12. Comparing figure 12 with figure 19, it can be seen that the magnitude of the wall pressure field obtained using the criteria in equation (29) is much lower than that computed using the criteria in equation (23). This is due to the fact that using the criteria in equation (29), only a small part of the wavenumber space domain was considered to numerically evaluate the Fourier integral in equation (4), as shown in figure 18. This results in a significant reduction in computational time as a considerably smaller number of wall plane waves need to be taken into account. However, the criteria in equation (23) should be used if sub-critical pressure gusts must also be taken into account.

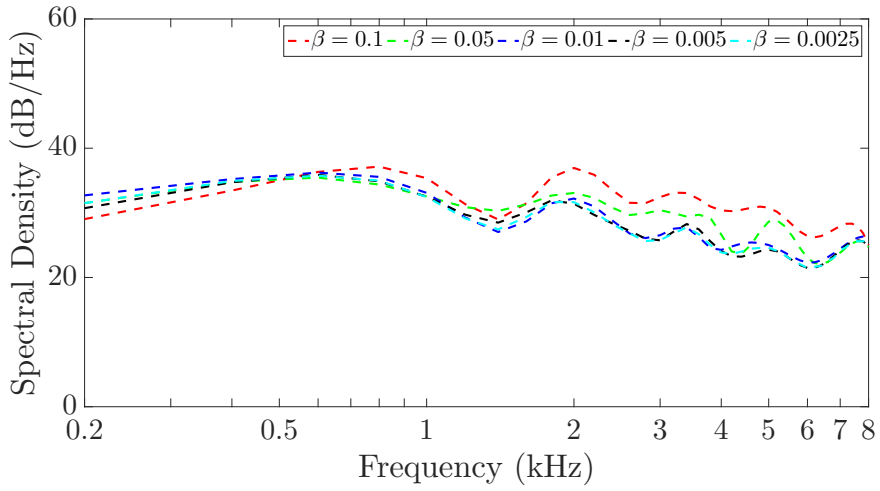

(a)

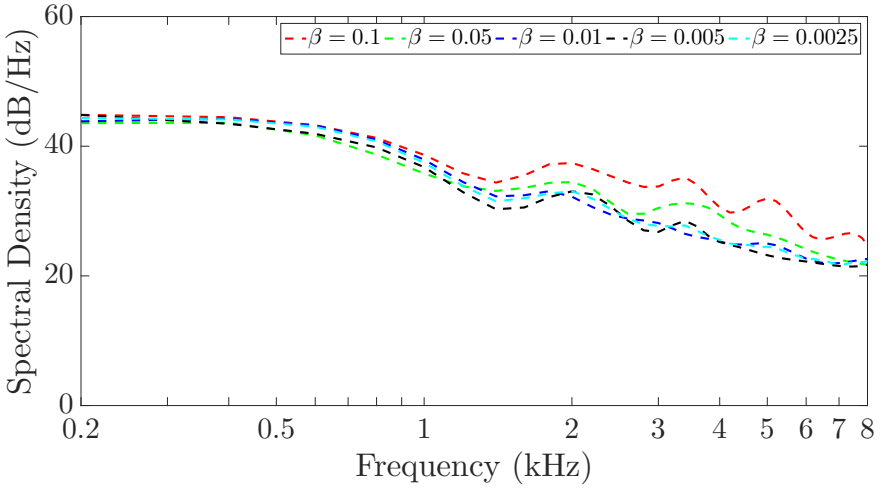

(b)

FIGURE 17 The effect of the wavenumber resolution on the far-field scattered pressure for the (a) Chase and (b) generalized Corcos models

A grid refinement study was conducted to find the appropriate mesh size. This study was performed on 10% of the full span of the plate and the cutoff wavenumbers in equation (29) were used. Five mesh sizes (6 mm, 3 mm, 2 mm, 1.5 mm and 1 mm) were considered with the same size in the streamwise and spanwise directions (i.e. $\Delta x = \Delta y$). Figure 20 shows that as the grid is refined, the computed solution approaches a converged value. As such, the 6 mm, 3 mm and 2 mm mesh sizes can be used for obtaining a converged scattered acoustic pressure up to 2.6 kHz, 4.6 kHz and 7.4 kHz, respectively. Hence, the 2 mm mesh was used to compute the results up to 7.4 kHz. Since both 1 mm and 1.5 mm meshes were able to produce converged results between 7.4 kHz and 8 kHz, the 1.5 mm mesh was exploited for the analysis in this upper frequency range. The power spectrum density of the scattered pressure is shown in figure 21 using the criteria in equations (23) and (29) corresponding to the superscripts [1] and [2], respectively. The results confirm that the sub-critical pressure gust does not contribute significantly to the scattered pressure in this case.

4.3 | Far-field noise prediction

The directivity of scattered acoustic pressure (Pa) from the flat plate at four discrete frequencies, obtained by ensemble averaging the scattered pressure over 30 realisations using the generalised Corcos model, are examined. Figure 22 shows that as the

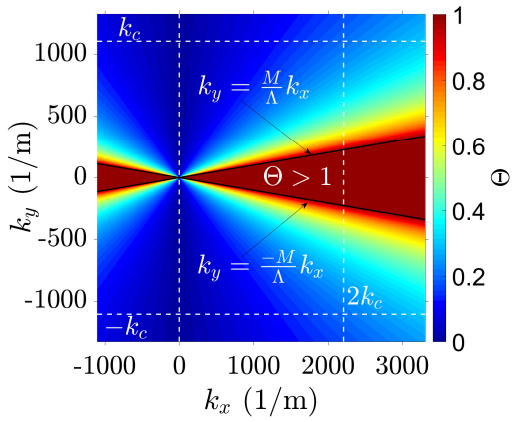

FIGURE 18 The wavenumber domain where Graham's parameter is greater or smaller than unity

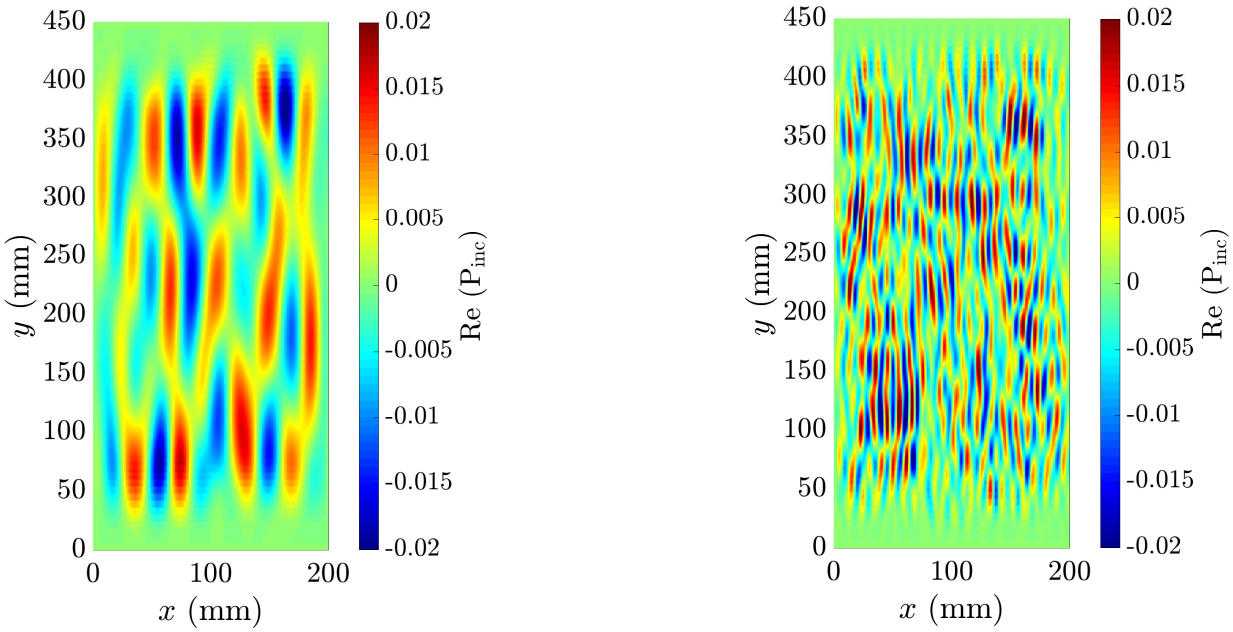

FIGURE 19 Two realisations of the wall pressure field at 0.6 kHz (left) and 2.2 kHz (right) using the Corcos model and the cutoff wavenumbers in equation (29)

frequency increases from 1 to 7 kHz, the sound pressure decreases and the direction of maximum noise shifts closer to the leading edge. At all frequencies it can be observed that there is no radiation in directions corresponding to 0° and 180°, attributed to the finiteness of the chord. Acoustic waves generated on opposite sides of the trailing edge are out of phase with the same magnitude. They travel along the surface of the airfoil until they arrive at the leading edge where they are diffracted. At this point, destructive interference leads to minimum noise being propagated in the upstream direction. This is consistent with the findings reported by Oberai et al.[3]. In addition, due to the fact that the chord is acoustically non compact at higher frequencies, the sound scattered by the trailing edge is back-scattered by the leading edge, resulting in multiple lobes in the directivity.

Figure 23 compares the scattered sound predicted using the proposed UWPW-BEM method with experimental and LES-BEM results. The lower and upper limits of the confidence interval in the measured spectrum are -1.14 and +1.01 dB/Hz, respectively. The UWPW-BEM results were obtained by ensemble averaging the scattered pressure over 30 realisations using the criteria in equation (29). In the hybrid LES-BEM approach, a correction of PSD_c is added to the far-field power spectral density for the

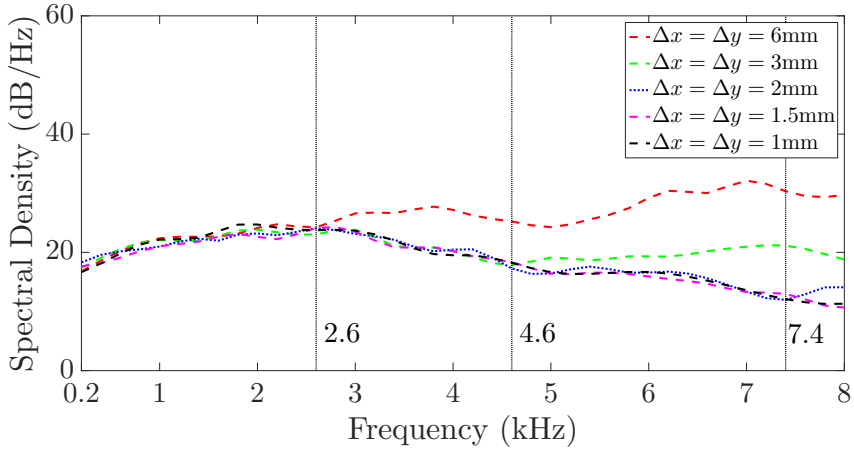

FIGURE 20 A grid refinement study using 10% of the span of the flat plate

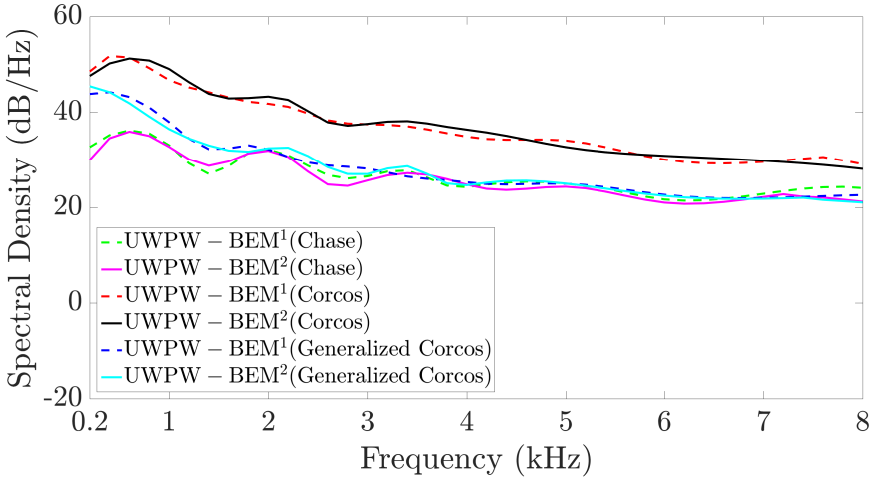

FIGURE 21 PSD of the far field acoustic response using two cutoff wavenumber criteria in y-direction. Superscripts [1] and [2] refer to criteria in equations (23) and (29) respectively

simulated span of the plate ($\mathrm{PSD_s}$) to estimate the power spectral density for the entire span of the plate ($\mathrm{PSD_t}$) as follows

$$\mathrm{PSD_t} = \mathrm{PSD_s} + \mathrm{PSD_c}. \tag{30}$$

The correction of $\mathrm{PSD_c}$ is given by[4]

$$\mathrm{PSD}_c = \begin{cases} 10\log\left(N_f\right), \frac{L_c'}{L_s} \leq \frac{1}{\sqrt{\pi}} \\ 10\log\left(\frac{L_c'}{L_s}\right) + 10\log\left(\sqrt{\pi}N_f\right), \frac{1}{\sqrt{\pi}} < \frac{L_c'}{L_s} < \frac{N_f}{\sqrt{\pi}} \\ 20\log\left(N_f\right), \frac{L_c'}{L_s} \geq \frac{N_f}{\sqrt{\pi}} \end{cases} \tag{31}$$

where N_f is the total number of spanwise segments in contact with flow, L_s is the length of the simulated span and L_c' is the spanwise coherence length. In both hybrid approaches, a periodic technique was implemented in the BEM model so that the problem was represented as a block Toeplitz system[48,49]. Using the Toeplitz structure, the computational time and storage requirements to construct and solve the linear system of equations in the BEM formulation were significantly reduced.

Figure 23 shows that the numerical results are in good agreement with experimental data at intermediate and high frequencies. However, there is a difference between the numerical and experimental results at low frequencies. It should be noted that the

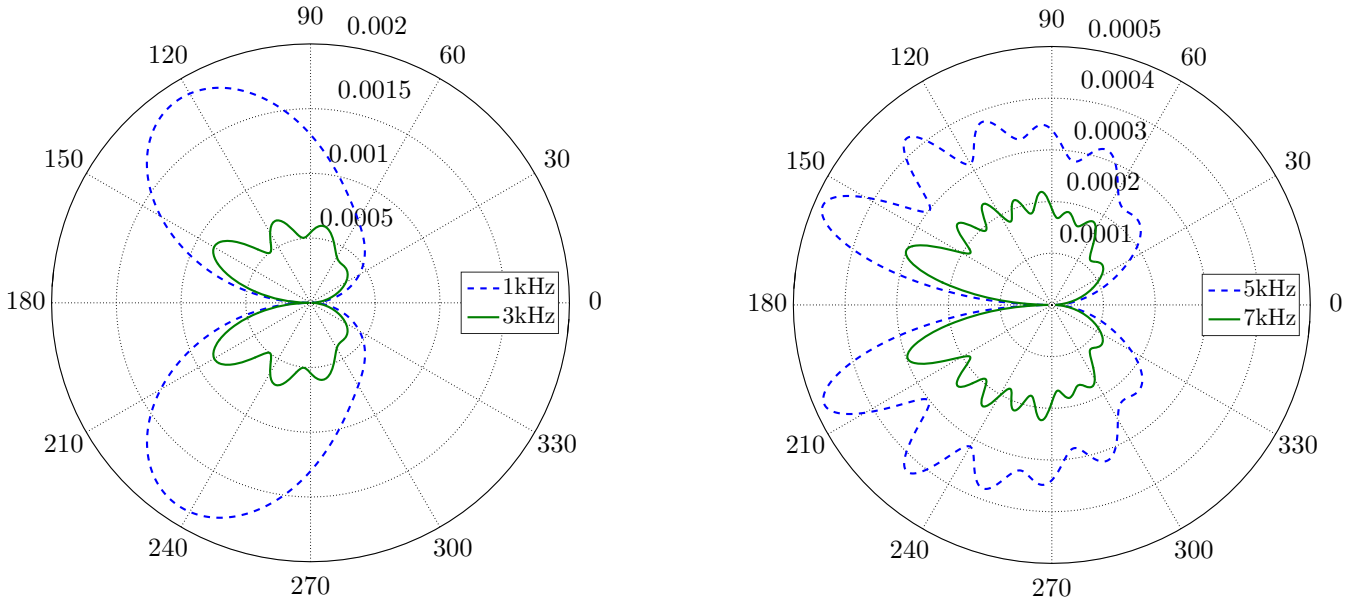

FIGURE 22 Directivity of the acoustic pressure on a circle lying in the mid-span of the plate with radius of 585 mm centred at the trailing edge at frequencies of 1 and 3 kHz (left), 5 and 7 kHz (right)

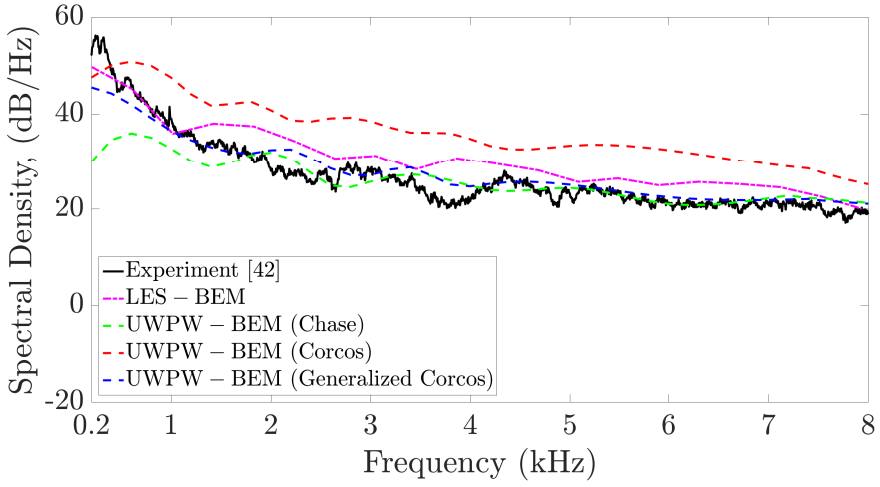

FIGURE 23 Comparison of experimental and numerical results for the far-field acoustic spectra

anechoic wind tunnel approximates a free field above approximately 250 Hz. Hence, experimental data below 250 Hz should be treated with caution because the test chamber could not provide a reflection free environment at low frequencies. In the experiment, the most significant source of low frequency noise is due to the shear layers that form at the side edges of the contraction outlet interacting with the plate leading edge. Another possible source of low frequency noise is due to the interaction of the shear layer with the collector located downstream of the test section. These low frequency noise sources do not exist in the numerical model. At low frequencies, the leading edge noise of the plate in turbulent flow is dominant. At high frequencies the trailing edge noise dominates the total generated noise.

The UWPW-BEM results are presented using the Chase, Corcos and generalized Corcos models. It has been previously reported that the Corcos model over predicts the pressure spectrum at low wavenumbers[37]. However, using the generalised Corcos model with filter orders of $m = 1$ and $n = 2$, the low wavenumbers are more accurately represented. Figure 23 shows that there is excellent agreement between the UWPW-BEM results based on the generalized Corcos model and those obtained from the experiment almost over the entire frequency range. The UWPW-BEM results based on the Chase model also agree

favourably with the experimental results above 2 kHz. However at low frequencies, the Chase model significantly under predicts the far-field sound pressure. The LES-BEM results are in good agreement with the measurements. However, the predicted spectral level is higher than the experimental data and UWPW-BEM results which could be due to over prediction of the velocity fluctuations in the LES simulation as shown in Figure 9. The discrepancy observed in Figure 23 could also be attributed to the sensitivity of the surface pressure wavenumber spectra to changes in spanwise mesh resolution. The spanwise resolution of the LES mesh could prevent the development and propagation of higher wavenumber content, thereby trapping extra flow energy at lower wavenumbers and frequencies[50].

5 | SUMMARY

An efficient numerical hybrid approach for flow noise prediction in which the computation of flow is decoupled from the computation of sound has been presented. A CFD solver based on RANS was exploited to simulate the fluid dynamics and an acoustic solver based on the BEM was implemented for the acoustic calculations. A RANS simulation was initially conducted to estimate TBL parameters. An uncorrelated wall plane wave technique was implemented to express the random wall pressure fluctuations. The pressure field was then applied directly as an input to a BEM solver to calculate the scattered acoustic field. The technique was employed to predict flow-induced noise by a sharp-edged flat plate in turbulent flow. Results were compared with those obtained from a high fidelity LES-BEM technique as well as with experimental data from literature, showing good agreement.

ACKNOWLEDGEMENTS

The authors would like to thank Dr Paul Dylejko for his useful suggestions and comments made during the course of this work. The first author would like to acknowledge the financial support from Defence Science and Technology Group. This work was performed in part on High Performance Computing Clusters (HPCC), Trentino and Lighthill, which are supported by the School of Mechanical and Manufacturing Engineering, University of New South Wales.

APENDIX A

AUTO SPECTRUM DENSITY FUNCTION

The Goody model

The empirical model of the auto spectrum density function of the pressure field is given by Goody[20]

$$\Psi_{pp}(\omega) = \frac{3\tau_w^2\delta\left(\frac{\omega\delta}{U_e}\right)^2}{U_e\left(0.5+\left(\frac{\omega\delta}{U_e}\right)^{0.75}\right)^{3.7}\left(1.1R_T^{-0.57}\left(\frac{\omega\delta}{U_e}\right)\right)^7} \tag{32}$$

where $R_T = U_\tau^2\delta/U_e\nu$ and U_e is the velocity at the boundary-layer edge.

APENDIX B

NORMALIZED CROSS SPECTRUM DENSITY FUNCTION

The Chase model

The Chase's normalized wavenumber-frequency model is given by Chase[23]

$$\tilde{\phi}_{pp}(k_x, k_y, \omega) = \frac{(2\pi)^3 \rho^2 U_\tau^3 \omega^2}{U_c^2 \phi(\omega)} \left(\frac{C_M k_x^2}{\left(K_+^2 + (b_M \delta)^{-2}\right)^{5/2}} + \frac{C_T |\mathbf{k}|^2}{\left(K_+^2 + (b_T \delta)^{-2}\right)^{5/2}} \right) \tag{33}$$

The required variables and constants are as follows

$$K_+^2 = \frac{(\omega - U_c k_x)^2}{h^2 U_\tau^2} + |\mathbf{k}|^2 \tag{34}$$

$$\phi(\omega) = \frac{(2\pi)^2 \rho^2 h U_\tau^4}{3\omega(1+\mu^2)} (C_M F_M + C_T F_T) \tag{35}$$

$$F_M = \frac{1 + \mu^2 \alpha_M^2 + \mu^4(\alpha_M^2 - 1)}{\left(\alpha_M^2 + \mu^2(\alpha_M^2 - 1)\right)^{3/2}} \tag{36}$$

$$F_T = \frac{1 + \alpha_T^2 + \mu^2(\alpha_T^2 - 1) + 2\mu^4(3\alpha_T^2 - 1)}{\left(\alpha_T^2 + \mu^2(\alpha_T^2 - 1)\right)^{3/2}} \tag{37}$$

$$\alpha_M^2 = 1 + \left(\frac{U_c}{b_M \omega \delta} \right)^2 \tag{38}$$

$$\alpha_T^2 = 1 + \left(\frac{U_c}{b_T \omega \delta} \right)^2 \tag{39}$$

$$\mu = \frac{h U_\tau}{U_c} \tag{40}$$

where δ is the boundary layer thickness, $|\mathbf{k}| = \sqrt{k_x^2 + k_y^2}$, $U_\tau = \sqrt{\tau_w / \rho}$ and τ_w is the wall shear stress. $C_M = 0.0745$, $C_T = 0.0475$, $b_M = 0.756$, $b_T = 0.378$ and $h = 3$.

The Corcos model

The Corcos normalized wavevector-frequency spectrum is given by Corcos[22]

$$\tilde{\phi}_{pp}(k_x, k_y, \omega) = \frac{4\alpha_x \alpha_y}{\left(\alpha_x^2 + \left(\frac{U_c k_x}{\omega} - 1 \right)^2 \right) \left(\alpha_y^2 + \left(\frac{U_c k_y}{\omega} \right)^2 \right)} \tag{41}$$

where $\alpha_x = 0.1$ and $\alpha_y = 0.77$.

The generalized Corcos model

The normalized wavevector-frequency spectrum of the generalized Corcos model is given by Caiazzo et al.[26]

$$\tilde{\phi}_{pp}(k_x, k_y, \omega) = \frac{\omega^2}{U_c^2} \frac{4 B_n(k_x) B_m(k_y)}{\left(\frac{-A_{k_x} A_{k_y} \alpha_\omega \beta_\omega}{nm} \right) \sum_{j=0}^{n-1} e^{-i\theta_j} \sum_{j=0}^{m-1} e^{-i\theta_j}} \tag{42}$$

$$B_n(k_x) = \frac{A_{k_x}}{1 + \left(\frac{k_x - k_\omega}{\alpha_\omega} \right)^{2n}} \tag{43}$$

$$B_n(k_y) = \frac{A_{k_y}}{1 + \left(\frac{k_y}{\beta_\omega}\right)^{2m}} \tag{44}$$

$$A_{k_x} = \frac{n \sin(\frac{\pi}{2n})}{\pi \alpha_\omega}; \qquad A_{k_y} = \frac{m \sin(\frac{\pi}{2m})}{\pi \beta_\omega} \tag{45}$$

$$\alpha_\omega = k_\omega \alpha_x; \qquad \beta_\omega = k_\omega \alpha_y; \qquad k_\omega = \frac{\omega}{U_c} \tag{46}$$

$$\theta_j = \frac{\pi}{2n}(1 + 2j) \tag{47}$$

References

1. Smits A. J, Marusic I. Wall-bounded turbulence. *Phys Today.* 2013;66(9):25-30.
2. Wang M, Moin P. Computation of trailing-edge flow and noise using large-eddy simulation. *AIAA J.* 2000;38:2201-2209.
3. Oberai A, Roknaldin F, Hughes T. J. R. Computational procedures for determining structural-acoustic response due to hydrodynamic sources. *Comput Method Appl M.* 2000;190:345-361.
4. Seo J.H, Moon Y.J. Aerodynamic noise prediction for long-span bodies. *J Sound Vib.* 2007;306(3-5):564-579.
5. Croaker P, Kessissoglou N, Kinns R, Marburg S. Fast low-storage method for evaluating Lighthill's volume quadrupoles. *AIAA J.* 2013;51(4):867–884.
6. Croaker P, Kessissoglou N, Marburg S. Aeroacoustic scattering using a particle accelerated computational fluid dynamics/boundary element technique. *AIAA J.* 2016;54(7):1-18.
7. Karimi M, Croaker P, Peake N, Kessissoglou N. Acoustic scattering for rotational and translational symmetric structures in nonuniform potential flow. *AIAA Journal.* 2017;:3318–3327.
8. Blake W. K. *A statistical description of pressure and velocity fields at the trailing edge of a flat strut.* DTNSRDC report 4241: David Taylor Naval Ship R & D Center, Maryland; 1975.
9. Moon Y.J, Seo J.H, Bae Y.M, Roger M, Becker S. A hybrid prediction method for low-subsonic turbulent flow noise. *Comput Fluids.* 2010;39:1125-1135.
10. Manoha E, Troff B, Sagaut P. Trailing-edge noise prediction using large-eddy simulation and acoustic analogy. *AIAA J.* 2000;38(4):575–583.
11. Bailly C, Lafon Ph, Candel S. Subsonic and supersonic jet noise predictions from statistical source models. *AIAA J.* 1997;35(11):1688–1696.
12. Peltier L, Hambric S. Estimating turbulent-boundary-layer wall-pressure spectra from CFD RANS solutions. *J Fluid Struct.* 2007;23(6):920–937.
13. Billson M, Eriksson L, Davidson L. Jet noise prediction using stochastic turbulence modeling. *9th AIAA/CEAS Aeroacoustics Conference and Exhibit*, 12-14 May 2003, Hilton Head, South Carolina, USA.
14. Lighthill M. J. On sound generated aerodynamically. *Proc Soc Roy Soc A.* 1952;211:564-587.
15. Bechara W, Bailly Ch, Lafon Ph, Candel S. Stochastic approach to noise modeling for free turbulent flows. *AIAA J.* 1994;32(3):455–463.
16. Ewert R. Broadband slat noise prediction based on CAA and stochastic sound sources from a fast random particle-mesh (RPM) method. *Comput Fluids.* 2008;37(4):369–387.

17. Lee Y. T, Blake W. K, Farabee T. M. Modeling of wall pressure fluctuations based on time mean flow field. *J Fluid Eng.* 2005;127(2):233–240.

18. Efimtsov B. Characteristics of the field of turbulent wall pressure-fluctuations at large Reynolds-numbers. *Soviet Physics Acoustics-USSR.* 1982;28(4):289–292.

19. Howe MS. On the structure of the turbulent boundary-layer wall pressure spectrum in the vicinity of the acoustic wavenumber. *Proc Soc Roy Soc A.* 1987, 389-401.

20. Goody M. Empirical spectral model of surface pressure fluctuations. *AIAA J.* 2004;42:1788-1793.

21. Rozenberg Y, Robert G., Moreau S. Wall-pressure spectral model including the adverse pressure gradient effects. *AIAA J.* 2012;50(10):2168–2179.

22. Corcos G. Resolution of pressure in turbulence. *J Acoust Soc Am.* 1963;35(2):192–199.

23. Chase D. The character of turbulent wall pressure spectrum at subconvective wavenumwave and a suggested comprehensive model. *J Sound Vib.* 1987;112:127-147.

24. Smol'yakov A, Tkachenko V. Model of a field of pseudosonic turbulent wall pressures and experimental data. *Soviet Physics (Acoustics).* 1991;37:627-631.

25. Miller T, Gallman J. M, Moeller M. J. Review of turbulent boundary-layer models for acoustic analysis. *J Aircraft.* 2012;49(6):1739–1754.

26. Caiazzo A, Amico R. D, Desmet W. A generalized Corcos model for modelling turbulent boundary layer wall pressure fluctuations. *J Sound Vib.* 2016;372:192 - 210.

27. Chen L, MacGillivray I. R. Prediction of trailing-edge noise based on Reynolds-averaged Navier-Stokes solution. *AIAA J.* 2014;52(12):2673–2682.

28. Albarracin C. A, Doolan C. J, Jones R. F, Hansen C. H, Brooks L. A, Teubner M. D. A RANS-based statistical noise model for trailing edge noise. *18th AIAA/CEAS Aeroacoustics Conference*, 4-6 June 2012, Colorado Springs, USA.

29. Maxit L. Simulation of the pressure field beneath a turbulent boundary layer using realizations of uncorrelated wall plane waves. *J Acoust Soc Am.* 2016;140(2):1268–1285.

30. Polacsek C, Burguburu S. Fan interaction noise predictions using rans-bem coupling. *Int J Aeroacoust.* 2005;4(1):153–167.

31. Croaker P, Kessissoglou N, Marburg S. Strongly singular and hypersingular integrals for aeroacoustic incident fields. *Int J Numer Methods Fluids.* 2015;77(5):274–318.

32. Ostertag J, Guidati S, Guidati G, Wagner S, Wilde A, Kalitzin N. Prediction and measurement of airframe noise on a generic body. *6th AIAA/CEAS Aeroacoustics Conference*, 12-14 June 2000, Hawaii, USA.

33. Khalighi Y, Mani A, Ham F, Moin P. Prediction of sound generated by complex flows at low Mach numbers. *AIAA J.* 2010;48(2):306–316.

34. Croaker P, Kessissoglou N, Kinns R, Marburg S. Fast Low-Storage Method for Evaluating Lighthill's Volume Quadrupoles. *AIAA J.* 2013;51(4):867–884.

35. Saad Y, Schultz M. H. GMRES: A generalized minimal residual algorithm for solving nonsymmetric linear systems. *Siam J Sci Stat Comp.* 1986;7(3):856–869.

36. Vos R, Farokhi S. *Introduction to transonic aerodynamics*. Berlin, Germany: Springer; 2015.

37. Graham WR. A comparison of models for the wavenumber–frequency spectrum of turbulent boundary layer pressures. *J Sound Vib.* 1997;206(4):541–565.

38. Marburg S, Nolte B. *Computational acoustics of noise propagation in fluids - finite and boundary element methods*. Berlin, Germany: Springer; 2008.

39. Versteeg H.K, Malalasekera W. *An introduction to computational fluid dynamics: The Finite Volume Method*. Pearson Education, Limited; 2011.

40. Wolf W. R, Azevedo J. L. F, Lele S. K. Effects of mean flow convection, quadrupole sources and vortex shedding on airfoil overall sound pressure level. *J Sound Vib.* 2013;332:6905-6912.

41. Moreau D. J, Brooks L, Doolan C. J. Broadband trailing edge noise from a sharp-edged strut. *J Acoust Soc Am.* 2011;129(5):2820-2829.

42. Moreau D. J., Brooks L, Doolan C. J. The effect of boundary layer type on trailing edge noise from sharp-edged flat plates at low-to-moderate Reynolds number. *J Sound Vib.* 2012;331(17):3976–3988.

43. Chakraborty P, Balachandar S, Ronald A. On the relationships between local vortex identification schemes. *J Fluid Mech.* 2005;535:189-214.

44. Hong C, Shin K. Modeling of wall pressure fluctuations for finite element structural analysis. *J Sound Vib.* 2010;329(10):1673–1685.

45. Amiet R.K. Acoustic radiation from an airfoil in a turbulent stream. *J Sound Vib.* 1975;41(4):407-420.

46. Graham J. M. R. Similarity rules for thin aerofoils in non-stationary subsonic flows. *J Fluid Mech.*1970 ;43(4):753-766.

47. Roger M, Moreau S. Extensions and limitations of analytical airfoil broadband noise models. *Int J Aeroacoust.* 2010;9(3):273–305.

48. Karimi M, Croaker P, Kessissoglou N. Boundary element solution for periodic acoustic problems. *J Sound Vib.* 2016;360:129-139.

49. Karimi M, Croaker P, Kessissoglou N. Acoustic scattering for 3D multi-directional periodic structures using the boundary element method. *J Acoust Soc Am.* 2017;141(1):313–323.

50. Park G, Moin P. Space-time characteristics of wall-pressure and wall shear-stress fluctuations in wall-modeled large eddy simulation. *Physical Review Fluids.* 2016;1(2):024404.